Biophysical Journal
Article

Viscoelastic phenotyping of red blood cells

Marta Gironella-Torrent,[1,2,*] Giulia Bergamaschi,[3] Raya Sorkin,[4] Gijs J. L. Wuite,[3] and Felix Ritort[1,5]
[1]Small Biosystems Lab, Condensed Matter Physics Department, University of Barcelona, Barcelona, Spain; [2]Department of Medical Biochemistry and Cell Biology, Institute of Biomedicine, The Sahlgrenska Academy, University of Gothenburg, Gothenburg, Sweden; [3]Department of Physics and Astronomy and LaserLab, Vrije Universiteit Amsterdam, Amsterdam, the Netherlands; [4]Raymond and Beverly Sackler Faculty of Exact Sciences, School of Chemistry, Tel Aviv University, Tel Aviv, Israel; and [5]Institut de Nanociència i Nanotecnologia (IN2UB), Universitat de Barcelona, Barcelona, Spain

ABSTRACT Red blood cells (RBCs) are the simplest cell types with complex dynamical and viscoelastic phenomenology. While the mechanical rigidity and the flickering noise of RBCs have been extensively investigated, an accurate determination of the constitutive equations of the relaxational kinetics is lacking. Here we measure the force relaxation of RBCs under different types of tensional and compressive extension-jump protocols by attaching an optically trapped bead to the RBC membrane. Relaxational kinetics follows linear response from 60 pN (tensional) to -20 pN (compressive) applied forces, exhibiting a triple exponential function with three well-separated timescales over four decades (0.01–100 s). While the fast timescale ($\tau_F \sim 0.02(1)$ s) corresponds to the relaxation of the membrane, the intermediate and slow timescales ($\tau_I = 4(1)$ s; $\tau_S = 70(8)$ s) likely arise from the cortex dynamics and the cytosol viscosity. Relaxation is highly heterogeneous across the RBC population, yet the three relaxation times are correlated, showing dynamical scaling. Finally, we find that glucose depletion and laser illumination of RBCs lead to faster triple exponential kinetics and RBC rigidification. Viscoelastic phenotyping is a promising dynamical biomarker applicable to other cell types and active systems.

SIGNIFICANCE This research shows the structured viscoelastic dynamics of red blood cells (RBCs) and highlights the significance of considering multiple timescales for understanding their mechanical behavior. The observed triple exponential relaxation behavior, coupled with the proposed viscoelastic model, provides valuable insights into the underlying processes governing RBC mechanics. Furthermore, our findings regarding the impact of glucose depletion and light illumination on RBC rigidity show how environmental factors affect RBC properties. Our results expand the current knowledge of RBC mechanics and pave the way for future investigations of relaxational phenomena in other cell types.

INTRODUCTION

Red blood cells (RBCs) are the most abundant and simplest cells in the human body. They are transported through the bloodstream to deliver oxygen to the body tissues. While they circulate through capillaries, RBCs are subject to mechanical deformation and stress. Capillaries can be as thin as half the RBC disk diameter (6–8 μm), causing RBCs to squeeze as they pass through. Mechanical properties of RBCs are tightly related to shape and composition, which are crucial for oxygen transport and delivery. They are also highly dependent on endogenous (e.g., genetic) and exogenous (e.g., physicochemical stresses, aging) factors and are determinants for homeostasis. If altered, they lead to diseases and disorders, such as hemolytic anemias and thrombosis. Therefore, RBC mechanical properties are key biomarkers for human health.

In humans, mature RBCs lack a nucleus to maximize the storage of hemoglobin and oxygen transport capacity. Moreover, the typical biconcave shape of RBCs increases their surface area, facilitating oxygen diffusion (1). The lifespan of human RBCs is about 115 days (2). During this period, they cyclically circulate in the bloodstream lasting for about a minute per cycle (3) and are subject to continuous deformation, leading to a variety of cell states (4).

Mechanical deformability dysfunction is directly related to diseases such as sickle cell anemia (5), malaria (6), and thalassemia (7). Moreover, during their lifespan, RBCs suffer from numerous age-dependent alterations that form the RBC aging phenotype, such as a decline of metabolic activity, cell shape modification (8), oxidative injury (9), and mechanical fatigue (10), among others (11). These alterations

---

Submitted August 9, 2023, and accepted for publication January 18, 2024.

*Correspondence: ritort@ub.edu

Editor: Baohua Ji.
https://doi.org/10.1016/j.bpj.2024.01.019

trigger erythrophagocytosis or the ingestion of RBCs by macrophages (12). It has been reported that most RBC dysfunctions lead to a rigidification of the cell (5–7,13,14).

RBCs are viscoelastic, showing complex time-dependent responses to external perturbations. Dynamical biomarkers such as frequency-dependent elastic moduli yield valuable information about their physiological state. In the past, the viscoelastic response of living cells and RBCs has been studied with techniques as diverse as micropipette aspiration (15–17), deformation in a flow (18–20), atomic force microscopy (21), acoustic force spectroscopy (22), optical magnetic twisting cytometry (23), deterministic lateral displacement devices (24), and laser optical tweezers (LOT) (25–28). These techniques have also been employed to study active polymer networks (29,30). The dynamical response of RBCs depends on the type of perturbation applied, the geometry of the experimental configuration, and the measured physicochemical property. Mechanical stiffness measurements have reported values that change by two orders of magnitude depending on the pulling orientation, the bond attachment type, and the probe's contact area. Noise correlation spectroscopy has emerged as an excellent technique to investigate rheological phenomena and activity of RBCs, e.g., using LOT (31–35). It is useful for measuring membrane fluctuations (flickering) in the high-frequency domain (subsecond timescale). In the low-frequency domain (≥ 1 s), active fluctuations and nonequilibrium phenomena are observed (30,32,36). RBC flickering has been shown to depend on the viscosity of the surrounding medium, demonstrating that flickering is an active process (37). The power spectrum of the flickering signal at low frequencies increases with ATP concentration, contributing to an average entropy production of thousands of k_BT/s per μm^2 of surface area (36,38). Therefore, a quantitative characterization of RBC relaxation in the low-frequency domain is key to a better understanding of RBC hemostasis (39).

Here, we carry out a new class of tensional and compressive extension-jump experiments in RBCs with optical tweezers and measure force relaxation over four decades (0.01–100 s). We discover a previously unknown triple exponential force relaxation with three well-separated timescales (fast, intermediate, and slow) that permits us to extract the constitutive parameters (stiffness and friction coefficient) of the dissipative processes in the RBC. The three timescales emerge from the underlying RBC architecture, providing a dynamical biomarker for RBC phenotyping based on viscoelastic relaxation experiments.

MATERIALS AND METHODS

Sample preparation

Human RBCs were freshly prepared before each experiment by finger-pricking of a healthy donor. Four microliters of blood were diluted in 1 mL of a PBS solution containing 130 mM NaCl, 20 mM K/Na phosphate buffer, 10 mM glucose, and 1 mg/mL BSA (32). Two types of beads were used for the experiments: polystyrene beads for nonspecific attachment (diameter 3 μm) and silica beads coated with concanavalin A (diameter 3 μm) for the specific attachments to the RBC. All materials were purchased at Sigma-Aldrich (St. Louis, Missouri, USA).

Experimental setup

Experiments were done in a miniaturized version of an optical tweezers instrument described in (40). Measurements were performed with highly stable miniaturized laser tweezers in the dual-trap mode, which consists of two counterpropagating laser beams focused on the same spot creating an optical trap. The instrument directly measures forces by linear momentum conservation. Piezo actuators bend the optical fibers and allow us to move the trap while measuring its position using a light lever that deflects 5% of the light to a position-sensitive detector. Force and trap position measurements are acquired at 1 kHz bandwidth. The experiments are performed in a microfluidics chamber made of two glass coverslips and two sheets of parafilm with three channels: the central one, where the optical trap and the micropipette are located; and two supplier channels, each one with a dispenser tube, to supply beads and RBCs. Details of the pipette and microfluidics chamber can be found in (41).

Experimental configuration

The RBC is vertically held between two micron-sized beads in the experimental configuration. One bead is immobilized on the tip of a micropipette by air suction, while the other is optically trapped. The pulling configuration requires the following steps. First, a bead from the first dispenser tube is captured in the central channel by the optical trap and moved close to the exit of the second dispenser tube where RBCs flow to the central channel. Second, a floating RBC in the central channel is brought in contact and attached to the optically trapped bead. A uniform laminar buffer flow is applied to the central channel to prevent RBCs from being optically trapped and damaged by the laser. Moreover, the flowed buffer cleans the working area from other RBCs that can interfere with the experiment. While applying the flow, the bead attached to the RBC is fixed to the tip of the micropipette. A second bead is captured in the trap and attached to the opposite extreme of the RBC. This second bead is used as the force probe for the experiments, Fig. 1 *a*. Further information can be found in (41).

Pulling experiments

For each RBC, a single force-distance curve is obtained. To compute the RBC stiffness, the relative trap position is converted into cell extension by subtracting the bead-trap displacement (F/k_b) from the measured trap-pipette distance with k_b the trap stiffness (40,41). Once the force-extension curve (FEC) is measured, a linear fit between 7.5 and 12.5 pN is performed by using the fit function of MATLAB. For forces below 5 pN, we observe a certain variability in the FECs due to the positioning of the contact point between the RBC and the lower bead. Significantly, this variation does not arise from the RBC itself but is a consequence of the distinct geometry in each experimental configuration. On the contrary, for higher forces (approximately 20 pN), tether formation is observed as a kink in the FEC, Fig. 1 *e*. To minimize variability, stiffness measurements are restricted to the force range between 7.5 and 12.5 pN.

Force-relaxation fits

Force-time relaxation curves (FRCs) were obtained by averaging force and time values in a logarithmic scale. The logarithmic averaged data are fitted to Eq. 1 with MATLAB using the fit function by imposing boundaries to the fitting parameters to minimize the computational time. The lower boundary for relaxation times is 0 s, and the upper boundary is 500 s. Regarding amplitudes, the lower boundary is $-\Delta F$ and the upper boundary is ΔF, with ΔF the magnitude of the force jump. The stationary force fitting parameter has

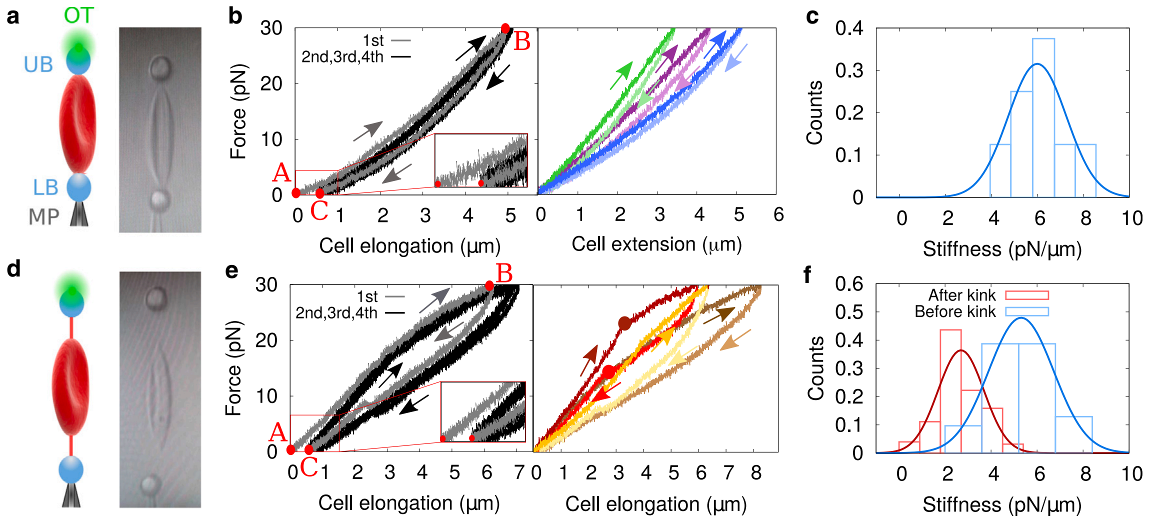

FIGURE 1 Pulling experiments on untethered (U) and tethered (T) RBCs. (*a*) Schematics and video image of our experimental configuration of the untethered population where the lower micro-sized bead (LB) is fixed on the tip of a micropipette (MP) and the upper bead (UB) is captured in the optical trap (OT) shown in green. (*b*) Left panel: first four FECs of an RBC without the tether. In gray, the first FEC shows a remanent elongation, and, in black, the three consecutive FECs overlap with each other. Right panel: FECs for three different RBCs, each one represented with a different color, the pulling curve (from 0 to 30 pN) is represented in dark color while the pushing curve (from 30 to 0 pN) is represented in a light color. (*c*) Histogram of untethered RBC stiffness obtained from the FECs of eight different RBCs. The stiffness is computed by performing a linear fit of the FEC between 7.5 and 12.5 pN. (*d*) Schematics and video images of the experimental configuration of the tethered population. In the image, the RBC presents two tethers, one attached to each bead, but it is also possible to have RBCs with only one tether in the lower or upper bead. (*e*) Left panel: first four FECs of an RBC with tether. In gray, the first FEC presents a remanent elongation and, in black, the consecutive three FECs that overlap with each other. Right panel: FECs for three different RBCs (*different colors*) in the presence of tether. The dark color represents the pulling curve from 0 to 30 pN, and the light color represents the pushing curve from 30 to 0 pN. (*f*) Stiffness histograms for the pulling FECs in the presence of tether. In blue, the stiffness values before the kink and, in red, the values after the kink (indicated as a dot in *e*, *right*). To see this figure in color, go online.

no boundaries. Fitting parameters with their uncertainty range are obtained using the confint function in MATLAB with 68% confidence.

RESULTS

In the experiments, a single RBC is attached to two polystyrene beads (3 μm diameter), each one at opposite ends of the cell (Fig. 1 *a*). The lower bead is immobilized by air suction on the tip of a micropipette, whereas the upper bead is captured in the optical trap. The experimental configuration requires a series of manual operations where beads are captured with the optical trap and attached to the RBC (see materials and methods). A flow is applied to the RBC to keep it far from the laser focus to avoid optical damage of the RBC by direct illumination (9,28). Two kinds of experiments have been performed: pulling and extension-jump experiments. In pulling experiments, the RBC is repeatedly stretched back and forth between a minimum and a maximum force, while the FEC is measured. In extension-jump experiments, one or more step-jumps are applied to the trap position (supporting material, section 2), and the FRC is measured.

Pulling experiments

Fig. 1 *b* (*left*) shows FECs of a single RBC repeatedly pulled between 0 and 30 pN. The first stretch-release pulling cycle (*left panel*, *gray*) systematically deviates from the following ones (*left panel*, *black*) in agreement with previous results (27). A fully relaxed RBC (point A) is mechanically stretched at ~1 pN/s up to 30 pN (point B). Then the trap is moved backward at the same speed until 0 pN, at which point a remanent elongation of ~ 0.5 μm is observed (point C and zoom). We interpret the remanent elongation as the irreversible orientation of the RBC that occurs in the first pulling cycle. The same phenomenon in a different context is observed in ferromagnetic materials where the initial magnetization curve differs from the rest due to the irreversible motion of the domain walls (42). Fig. 1 *b* (*right panel*) shows FECs for three different RBCs, which present mechanical hysteresis between the stretching (*dark color*) and releasing (*light color*) parts of the cycle (*upward* versus *downward arrows*). FECs show cell-to-cell variability indicating the heterogeneous mechanical response of the RBC population. From the FECs, we also extracted the (elongational) stiffness of the RBCs defined as the slope of the FEC between 7.5 and 12.5 pN (Fig. 1 *c*). The mean value (6.1 ± 1.3) pN/μm is compatible with previous experimental and simulation results with LOT (26). Moreover, we have obtained a compatible result of 7.6(3) pN/μm by computing the inverse of the creep compliance evaluated at 1 s, which is a more standard method to measure the cell stiffness (Fig. S1).

Sometimes, a tether forms at sufficiently high forces (around 25–30 pN). This observation is in accordance with the results obtained through micropipette aspiration (43). This is shown in Fig. 1 *d* where two tethers, each at one side of the RBC, are extruded above $\simeq 20$ pN. We have also observed cases where a single tether is extruded in one of the two sides only (indistinctly). Fig. 1 *e* (*left*) shows the first five pulling cycles of a single RBC in the presence of a tether. As in the untethered case, a similar remanent elongation (~ 0.5 μm) is observed after the first pulling cycle (Fig. 1 *e*, *left*, zoom), while Fig. 1 *e* (*right*) shows FECs for three different RBCs with tether formation.

The FECs with tether show higher hysteresis than those without tether (Fig. 1, *b* and *e*, *right*). Tether formation is observed as the detachment of one of the two beads from the cell body at a given force. Concomitantly, a kink appears in the FEC at that force where the stiffness drops. The same phenomenon is observed in the releasing process: a kink appears in the FEC upon tether absorption by the cell membrane. RBCs with a tether also show cell-to-cell variability and heterogeneous mechanical response across the RBC population (Fig. 1 *e*, *right*). Tether extrusion and absorption are cooperative processes at characteristic forces (*maroon* and *red dots*, respectively in Fig. 1 *e*, *right*). Tether formation is an irreversible process with hysteresis: tether extrusion occurs at forces higher than tether absorption (Fig. S2).

We also carried out experiments using beads of different materials (silica and polystyrene), sizes (3 and 6 μm diameter), and functionalized with concanavalin A, which specifically attaches to the RBC spectrin network, finding similar results (Fig. S3). In particular, we also found the same spread in cell-to-cell variability as for the case of nonspecific attachments, showing that heterogeneous mechanical response is an intrinsic feature of RBCs (Fig. S4).

Force-relaxation experiments

RBCs have a complex architecture consisting of two major structures: the membrane lipid bilayer and the 2D spectrin-actin network. One might identify structural contributions to the overall relaxation from mechanical stretching experiments. Here, we combine different kinds of extension-jump protocols and identify three well-separated and reproducible timescales in RBCs over four decades (0.01–300 s).

Two kinds of stepwise extension-jump protocols have been implemented, trotter and ladder (Fig. 2 *a*). Extension jumps are applied by instantaneously moving the trap position by $\Delta\lambda$ ($\sim 1 - 3$ μm) (Fig. S5). $\Delta\lambda > 0$ for tensional jumps (Fig. 2 *a*, *upper panels*) while $\Delta\lambda < 0$ for compressive jumps (Fig. 2 *a*, *lower panels*). The time between consecutive jumps is fixed to $\tau_0 = 5$ min (Fig. 2 *a*, *bottom axis*). The trap displacement $\Delta\lambda$ causes a force jump, $\Delta F = F_f - F_i$, where F_i is the initial force before the jump, and F_f is the force immediately after the jump (Fig. 2 *b*). FRCs are subsequently measured during $\tau_0 = 5$ min (Fig. 2 *b*). We label relaxation curves by ΔF, being positive (negative) for tensional (compressive) jumps. In trotter-type protocols, a single extension jump is applied (Fig. 2 *a*, *brown* and *dark green*) and FRCs measured (Fig. 2

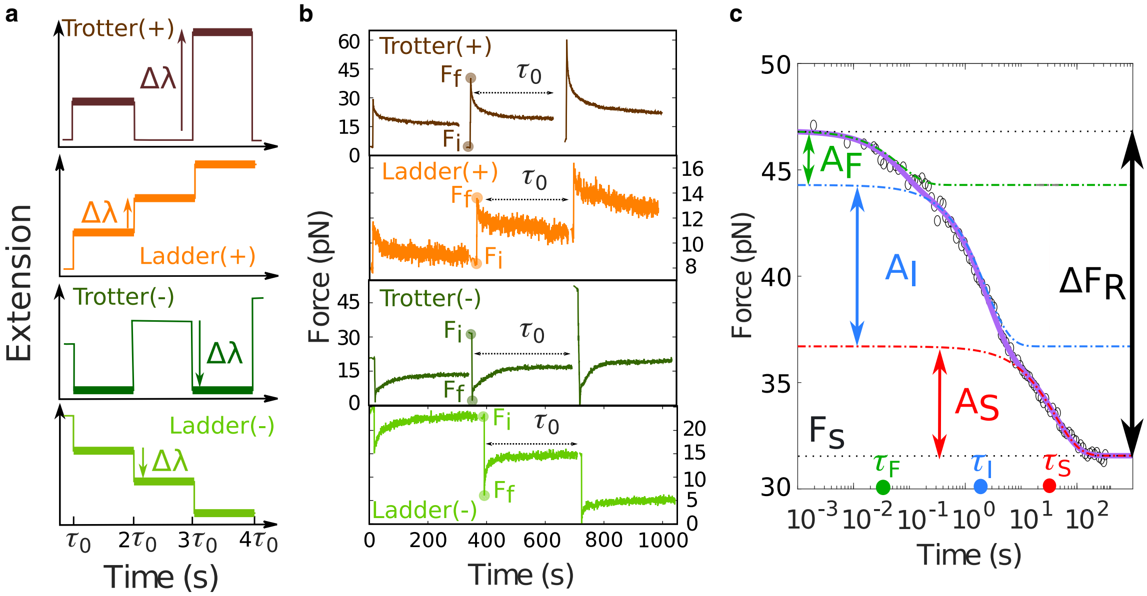

FIGURE 2 Protocols, FRCs, and triple exponential fit. (*a*) Schematic representation of trap displacement versus time for the different protocols (trotter(+), ladder(+), trotter(−), and ladder(−)). In thick lines, the time windows during which measurements are performed. The arrow next to $\Delta\lambda$ indicates the direction of the jump. (*b*) Three FRCs for each of the four different protocols in (*a*). Initial and final forces are indicated with big dots in the second FRC of each panel, defining the force jump $\Delta F = F_f - F_i$. (*c*) FRC in normal-log scale. Data points were obtained by average filtering. The fitting curve Eq. 1 is shown in purple. Parameters are shown for the fast (A_F and τ_F, *green*), intermediate (A_I and τ_I, *blue*), and slow (A_S and τ_S, *red*) processes. The stationary force, F_s, is shown as a black dotted line at the bottom. To see this figure in color, go online.

b, *brown* and *dark green*). The initial (final) force stays close to zero (< 5 pN) for tensional (compressive) jumps. In ladder-type protocols, extension jumps are consecutively applied (Fig. 2 in *orange* and *light green*), and FRCs measured at every ladder step (Fig. 2 *b*, *orange* and *light green*). In all protocols, several jumps (between two and five) of varying amplitude (ΔF) were applied, the total experimental time per RBC being approximately half an hour. FRCs in Fig. 2 *b* show a viscoelastic response over minutes upon RBC deformation. For tensional jumps ($\Delta\lambda$, $\Delta F > 0$, *upper panels*), force monotonically decreases with time, indicating RBC expansion. For compressive jumps ($\Delta\lambda$, $\Delta F < 0$, *lower panels*), force monotonically increases with time, indicating RBC contraction. In all protocols, FRCs relax toward a stationary force F_S that is higher (lower) than the initial force F_i for tensional (compressive) protocols.

Since the pioneering studies by Evans and Hochmuth (44) on RBC membrane viscoelasticity, a significant volume of research has been dedicated to exploring the shear modulus, viscoelastic properties, and relaxation dynamics. Most of the literature on RBC relaxation (15,18,19,25,45–48) reports that RBCs regain their shape in a time-dependent manner, exhibiting a characteristic single or double exponential behavior consistent with the viscoelastic solid model. Power laws have been also employed to fit the data (27,33,49–51). It is worth noting that the tensile/compressive deformations can also be referred to as loading/relaxation phases. Remarkably, and in contrast with these studies, we observe that FRCs show a triple exponential behavior (Fig. 2 *c*),

$$F(t) = A_F e^{-t/\tau_F} + A_I e^{-t/\tau_I} + A_S e^{-t/\tau_S} + F_s \qquad (1)$$

where $F_s = F(t \to \infty)$ and the A values and τ values define amplitudes and relaxation times of the fast (A_F, τ_F), intermediate (A_I, τ_I), and slow (A_S, τ_S) processes. The triple exponential relaxation is also apparent in relaxation experiments at constant force, where the force is jumped to a preset value that is kept constant using a feedback loop at 1 kHz, and the trap position relaxation is monitored (supporting material, section 2.2).

In Fig. 2 *c* we illustrate the parameters of the triple exponential for one relaxation curve of the trotter(+) type. A crucial feature of the FRC is the recovery force ΔF_R, defined as the total force change during the relaxation. From Eq. 1, $\Delta F_R = F(t = 0) - F_s = A_F + A_I + A_S$ (Fig. 2 *c*). ΔF_R measures the viscoelastic response of the RBC after it has been deformed. Notice that $\Delta F_R = 0$ would indicate a purely elastic response. We find that ΔF_R is approximately $\Delta F/2$, being positive (negative) for tensional (compressive) deformations exhibiting a viscoelastic response. Viscoelastic behavior has been previously reported in RBCs (26), epithelial cells (52), and shape memory polymers (53). Fig. 3 shows four selected FRCs with different protocols without a tether (Fig. 3 *a*) and with tether extrusion (Fig. 3 *b*), together with their fits to Eq. 1 (*black curves*). FRCs are qualitatively the same and a triple exponential is needed to fit the data in all cases. While other functions such as a double exponential and a stretched exponential fit the relaxational curves in some conditions, they do not consistently fit all the data (Figs. S6 and S7). A detailed statistical analysis of the fitting quality of the triple exponential function is shown in the supporting material (Fig. S8; Tables S1 and S2).

Fig. 4 shows all parameters of the fits (amplitudes and relaxation times) plotted versus the force jump ΔF. Results have been averaged over the different protocols (trotter(+)

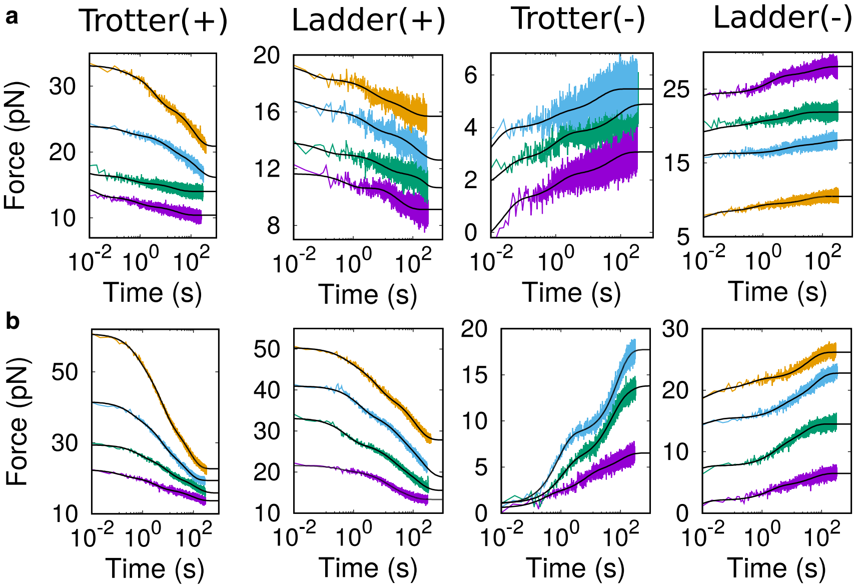

FIGURE 3 Experimental FRCs for the four different protocols. Force versus time in normal-log scale. Each panel shows the raw data (*different colors*) and their corresponding triple exponential fits Eq. 1 (*black*) for the four different protocols of Fig. 2. Each color represents a relaxation curve with a different ΔF. (*a*) For the untethered population and (*b*) for the tethered population. To see this figure in color, go online.

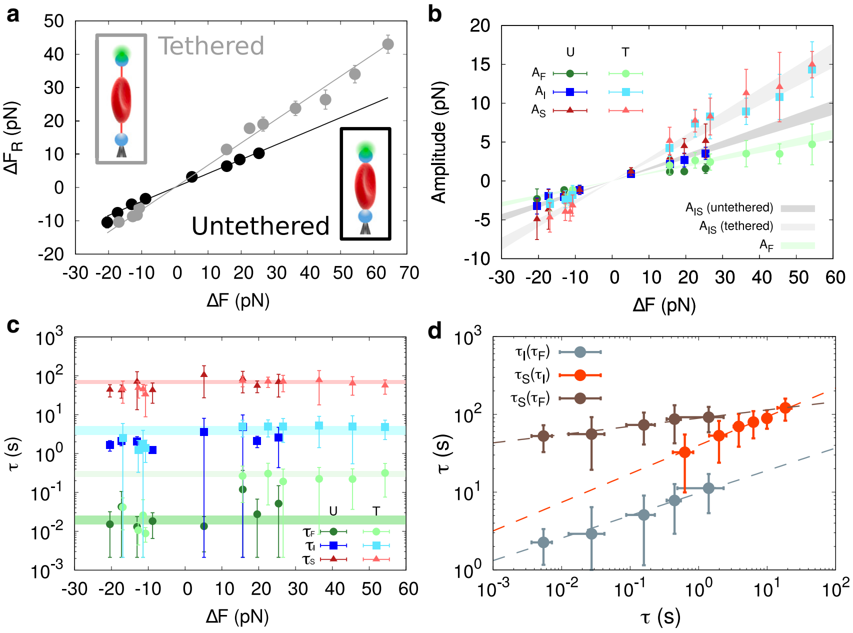

FIGURE 4 Recovery forces, amplitudes, and relaxation times. (*a*) Recovery force ΔF_R versus ΔF. In gray, the tethered case, and, in black, the untethered case. (*b*) Amplitudes versus ΔF for both types of RBC populations. In dark color, the untethered case (U) and, in light color, the tethered case (T). Green represents the fast amplitude, blue represents the intermediate amplitude, and red represents the slow amplitude. (*c*) Characteristic times versus ΔF for both tethered and untethered cases. In dark color, the untethered (U) case and, in light color, the tethered (T) case. Green represents the fast time τ_F, blue represents the intermediate time τ_I, and red represents the slow time τ_S. (*d*) Dynamical scaling for the three characteristic times taken over all experimental data (U and T). The error bars are defined as the statistical error of the average values over 3–5 different RBCs. To see this figure in color, go online.

with ladder(+) for $\Delta F > 0$ and trotter(−) with ladder(−) for $\Delta F < 0$). ΔF_R and the amplitudes $A_F, A_I,$ and A_s show a linear dependence with ΔF (Fig. 4, *a* and *b*). The same result is obtained for each protocol independently (Fig. S9). At a closer inspection, fitting parameters show a systematic difference between untethered and tethered RBCs. Therefore, these are shown separately for each case, every point being the average over three to six RBCs. In Fig. 4 *a*, we plot ΔF_R versus ΔF, untethered (U, *black circles*) and tethered (T, *gray circles*). A linear relation is found in both cases, $\Delta F_R = 0.42(2)\Delta F$ (untethered) and $\Delta F_R = 0.67(2)\Delta F$ (tethered) showing higher viscous response (i.e., larger ΔF_R) for tethered RBCs. The higher viscosity of the extruded tether leads to the higher hysteresis observed in the FECs (Fig. 1 *e*). Tether extrusion occurs at around 25 pN, so measurements for the untethered case were limited to force jumps $\Delta F < 25$ pN. Fig. 4 *b* shows the three amplitudes A_F (*green circles*), A_I (*blue squares*), and A_S (*red triangles*) plotted versus ΔF averaged over the different protocols. Again, a linear relation is found for the three amplitudes in the tethered (T, *light color*) and untethered (U, *dark color*) cases. Moreover, A_I and A_S (*blue* and *red symbols*) show similar linear slopes but differ from those for A_F (*green symbols*). Indeed, amplitudes A_I and A_S are compatible for the tethered and untethered cases. A single linear fit to A_I and A_S for all data gives $A_{IS} = 0.27(3)\Delta F$ (tether, *light gray area*) and $A_{IS} = 0.15(2)\Delta F$ (untethered, *dark gray area*). In contrast, for the fast amplitude A_F, similar values are obtained for the untethered (*dark green*) and tethered (*light green*) cases, $A_F = 0.11(1)\Delta F$ (*light green area*). We hypothesize that the fast process arises from the viscoelastic response between the bead and the RBC at the local contact area, for both tethered and untethered RBCs. Instead, the difference in A_{IS} between untethered and tethered suggests that the intermediate and slow processes depend on the different morphology of the RBC in the two cases (video images in Fig. 1, *a* and *d*). The fact $A_\mathrm{I} \simeq A_\mathrm{S} \equiv A_\mathrm{IS}$ is indicative of two equally stiff responsive viscoelastic elements connected in parallel (see next section).

Further information can be obtained from the relaxation times $\tau_F, \tau_I,$ and τ_S. The results are shown in Fig. 4 *c*. Remarkably, we find three distinct well-separated timescales independent of ΔF and the protocol. Moreover, these timescales are the same for tethered and untethered RBCs, except for τ_F for $\Delta F > 0$, which is larger for the tethered case (*light green* versus *dark green circles* for $\Delta F > 0$ in Fig. 4 *c*). Tether extrusion ($\Delta F > 0$) causes the RBC's membrane to flow from the RBC body toward the growing tether. The mass exchange process during the flow slows down the fast process by increasing τ_F. In fact, upon retraction of the RBC ($\Delta F < 0$), the tether is not absorbed, so τ_F remains unchanged for the untethered and tethered RBCs (*leftmost green points* in Fig. 4 *c*). Video images of the RBC's retraction show that the RBC's body does not fully absorb the tether, reducing the mass flow from the tether to the RBC. The irreversible flow of the membrane upon tether extrusion and retraction leads to the asymmetry of τ_F between $\Delta F > 0$ (Video S1, supporting material, section 2.7) and $\Delta F < 0$ (Video S2, supporting material, section 2.7). Averaging the values of τ_F over $\Delta F > 0$, we get $\tau_F(\Delta F > 0) = 0.30(5)$ s for the T case (*light green band*), whereas for the U case (all ΔF) and T case we get $\tau_F(\Delta F < 0) = 0.020(5)$ s (*dark green band*). By averaging τ_I, τ_S over T, U, and ΔF, we get $\tau_I = 4(1)$ s (*cyan band*) or

$\tau_S = 70(8)$ s (*light red band*). While τ_F and τ_I can be linked to the relaxation of the cell membrane, τ_S corresponds to the relaxation of the RBC's body, which takes significantly more time.

Remarkably, timescales τ_F, τ_I, and τ_S exhibit a strong heterogeneity across the RBC population throughout the experimental data (U and T), varying over several orders of magnitude. Despite this variability, timescales are strongly correlated, showing dynamical scaling. Fig. 4 *d* shows the three timescales plotted relative to each other. Timescales are power-law correlated, a signature of dynamic scaling, $\tau_i = \alpha\tau_j^{\beta}$ with $i,j = F,I,S$ and $\alpha, \beta > 0$. We obtain $\tau_I = 10(1)\tau_F^{0.29(2)}$ (*gray points*), $\tau_S = 40(2)\tau_I^{0.37(2)}$ (*orange points*), and $\tau_S = 89(3)\tau_F^{0.11(1)}$ (*brown points*).

Viscoelastic model

The triple exponential relaxation Eq. 1 can be reproduced by a viscoelastic model that combines the bead in the optical trap of stiffness k_b with a Maxwell-Wiechert configuration for the RBC. The latter consists of four elements: one spring of stiffness k_{RBC} and three spring-dashpots of stiffness, k_F, k_I, and k_S, and friction coefficients γ_F, γ_I, and γ_S, which are connected in parallel (Fig. 5). The model can be analytically solved (supporting material, section 2.3) under the approximation of timescale separation $\tau_F \ll \tau_I \ll \tau_S$ as observed in the experiments. We get,

$$\Delta F_R = \frac{\Delta F}{\left(1 + \frac{k_{RBC}}{k_b}\right)\left(1 + \frac{k_{RBC}}{k_{\parallel}}\right)} \tag{2}$$

$$A_i = \frac{k_i}{k_{RBC} + k_{\parallel}}\Delta F \tag{3}$$

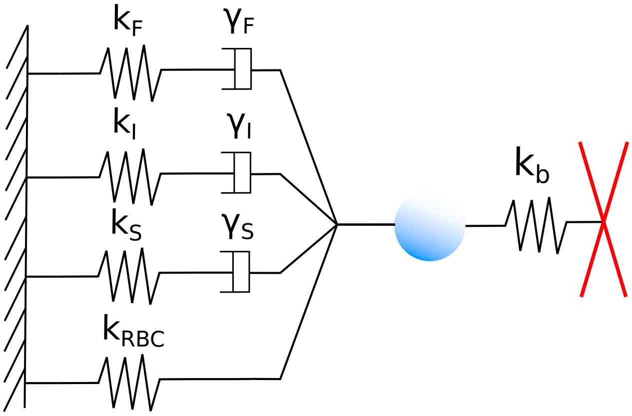

FIGURE 5 Schematics of the viscoelastic model. The RBC contribution is represented in the left side of the bead with three spring-dashpot elements and a single spring element connected in parallel. The optical trap is modeled as a spring on the right side of the bead. For more details, see supporting material, section 2.3, and Fig. S14. To see this figure in color, go online.

$$\tau_i = \frac{k_{RBC} + k_b + k_{\parallel}}{k_i(k_{RBC} + k_b + k_{\parallel} - k_i)}\gamma_i \tag{4}$$

with $i \equiv F,I,S$ and $k_{\parallel} = k_F + k_I + k_S$. Using the values of k_{RBC} obtained in the pulling experiments (Fig. 1, *c* and *f*), we can solve the equations and determine the six parameters $k_F, k_I, k_S, \gamma_F, \gamma_I$, and γ_S for the U and T cases. Results are summarized in Table 1. We remark on three results. First, γ_F for the T case is 10 times larger than for the U case, which we interpret as the additional friction caused by the tether on the RBC relaxation. Second, parameters for the I, and S spring-dashpot elements are equal for the U and T cases, indicating that the I and S processes correspond to the cell body relaxation, which is unaffected by tether formation. While the stiffnesses k_I and k_S are similar, friction coefficients γ_I and γ_S differ by a factor of 20, being also 100–1000 times larger than γ_F. The high γ_I, γ_S values explain the slow relaxation kinetics (up to tens of minutes) observed in the FRCs. This phenomenology conforms with the strong violations of the fluctuation-dissipation theorem observed at low frequencies in flickering noise experiments (36).

Rigidification of treated and irradiated RBCs

Under environmental damage, RBCs suffer structural modifications changing shape, and developing membrane instabilities. Fig. 6 *a* shows images of an RBC after partially depleting glucose and, consequently, ATP. RBCs were treated by incubating in a glucose-free buffer at 37°C for 20 h (48 h are needed for full depletion (36)). ATP is essential for RBC activity and membrane stability. ATP depletion prevents the dissociation/reassociation activity in the membrane cortex, and the spectrin network is rigidified (54–56). As shown in Fig. 6 *a*, RBCs develop membrane spikes with a star-like geometry (echinocyte). We have repeated the pulling experiments in this condition, finding much less stable RBC-bead attachments and RBC rigidification in the U ($k_{RBC} = 13(3)$ pN/μm, Fig. S15) and T ($k_{RBC} = 6(1)$ pN/μm) cases (Fig. 6 *b*). The values of k_{RBC} in treated and untreated RBCs for the untethered case are compatible with previous results (57), and in the same range of the stiffness of gosht RBC ~2 pN/μm (58). Interestingly, treated RBCs mostly exhibit tether formation in relaxation experiments, indicating membrane instability caused by changes in the relative area difference between the two leaflets of the lipid

TABLE 1 Fitting parameters of the viscoelastic model

pN/μm	k_{RBC}	$k_{\parallel}$	k_F	k_I	k_S
U	6.1(13)	5.3(1)	1.3(1)	2.0(1)	2.0(1)
T	2.7(6)	6.4(4)	1.0(1)	2.7(5)	2.7(5)

pN·s/μm	γ_F	γ_I	γ_S
U	0.025(3)	7.8(6)	136(12)
T	0.29(2)	10.2(7)	179(13)

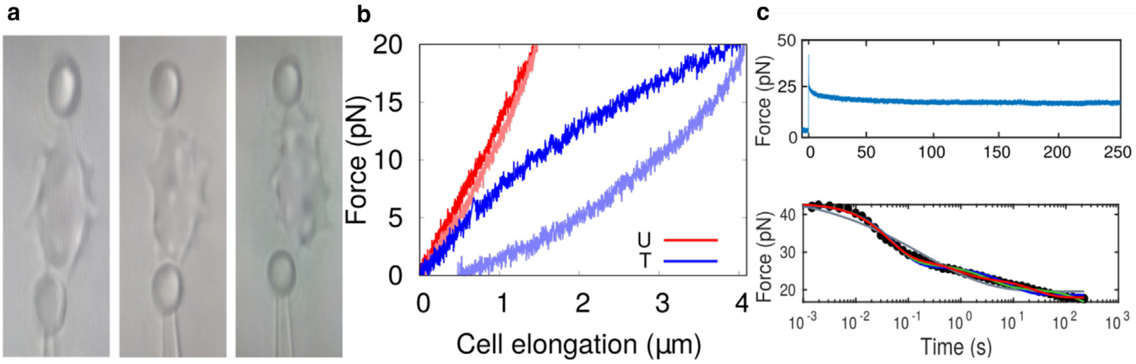

FIGURE 6 ATP-depleted RBC. (*a*) Three images of ATP-depleted RBC in echinocyte form. (*b*) Pulling cycles for a representative untethered (U, *red*) and tethered (T, *blue*) RBC. (*c*) Top panel: typical force-relaxation curve. Bottom panel: relaxation curve together with its fits to a triple exponential (*red*), triple exponential with $A_I = A_S$ (*green*), double exponential (*blue*), and stretched exponential (*gray*). Results are shown for a representative RBC and are reproducible over different RBCs. To see this figure in color, go online.

bilayer, which trigger the echinocyte transformation at low levels of ATP (54). In addition, it has been reported (59) that ATP is crucial for the recovery of mechanical properties in RBCs after tether extrusion. This is because ATP depletion impedes complete retraction and promotes subsequent extrusion. Again, all FRCs show a viscoelastic linear response with a triple exponential Eq. 1 (Figs. 6 *c* and S7). We find a slightly higher viscoelastic response $\Delta F_R = 0.71(2)\Delta F$ (Fig. S16 *a*) but lower intermediate and slow amplitudes ($A_{IS} = 0.20(3)\Delta F$, Fig. S16 *b*) compared with the previously shown untreated T case ($A_{IS} = 0.27(3)\Delta F$). In contrast, the fast amplitude triplicates its value ($A_F = 0.31(3)\Delta F$) compared with the untreated T case ($A_F = 0.11(1)\Delta F$). The relaxation timescales remain ΔF independent in agreement with linear response ($\tau_F = 0.029(2)$ s, $\tau_I = 1(1)$ s, $\tau_S = 41(3)$ s) but decrease relative to the untreated T case ($\tau_F = 0.30(5)$ s, $\tau_I = 4(1)$ s, $\tau_S = 70(8)$ s) as reported in previous studies where more than a single timescale is observed (48) (Fig. S16 *c*). Table S5 shows the recovery force, amplitudes, and relaxation times for the treated and untreated cases. This finding is consistent with the observation of faster extrusion of RBC tethers in the absence of ATP (59) and the substantially lower entropy production of passivated RBCs (38). From Eqs. 2, 3, and 4 we have extracted the viscoelastic parameters (Table 2). We find that the stiffnesses increase and the friction coefficients decrease relative to the untreated case, leading to RBC rigidification consistently with previous findings (32).

In another set of experiments, we studied the irradiation effect of the laser on the RBC at normal power ($\lambda = 845$ nm, $P \sim 80$ mW). This kind of damage is relevant in radiation therapies for cancer treatment (9). In Video S3, supporting material, section 2.7, we show the effect of infrared light on an RBC directly captured in the optical trap. Upon direct illumination, the RBC collapses after approximately 30 s. We have investigated the effect of the optical trap in the less invasive configuration of the pulling experiments (Fig. 1, *a* and *d*) where the RBC approaches the focus of the optical trap at low forces. We have carried out the experiments shown in Fig. 1 *b* for untethered RBCs to explore the cumulative effect of light on the RBC after repeated pulling cycles. As shown in Fig. 7 *a*, RBC elongation shortens at every cycle showing that RBCs rigidify upon light exposure at a rate of 0.077(4) pN/μm per pulling cycle, approximately doubling every $\sim$30 min, Fig. 7 *b*. Irradiation effects mainly occur at low forces during a pulling cycle, being residual when the RBC is pulled far from the light trap. To confirm this we have implemented a pulling protocol where we wait at zero force for a given time in two conditions: laser switched on at the normal power or at a very low trapping power ($P \sim 16$ mW). For the lower power the shortening is less apparent, demonstrating the direct effect of light on RBC stiffening (Fig. 7 *a*, *inset*). A similar effect has been observed in RBC stretching experiments using electric fields (10). It has also been reported that repeated stretching cycles might induce ATP loss from the RBC, which has membrane channels that let ATP go out when the cell is stretched (54). Another effect that could contribute is vesiculation: as the RBC loses ATP and is mechanically deformed, the membrane area can decrease (60). In fact, upon stretching without the laser effect (Fig. 7 *a*, *inset*, *blue colors*, laser OFF), a shortening of the extension is observed but of lesser magnitude than that observed with normal laser ON conditions. We conclude that laser illumination contributes to stiffening the RBC.

TABLE 2 Viscoelastic model parameters for treated RBCs with tether (T)

pN/ μm	k_{RBC}	$k_{\parallel}$	k_F	k_I	k_S
T	6(2)	8.9(4)	3.7(6)	2.6(3)	2.6(3)

pN·s/μm	γ_F	γ_I	γ_s
T	0.10(2)	2.5(3)	101(10)

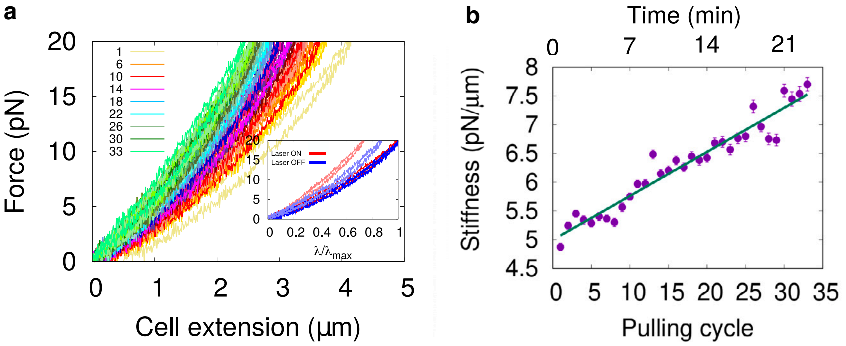

FIGURE 7 Laser effect in RBCs. (*a*) FECs of an RBC over time. Each color represents a different pulling cycle and the index on the legend is the cycle number. Inset: FEC of an RBC with and without the laser effect. Dark colors represent the second pulling cycle, and light colors represent another pulling cycle after 45 min. Stiffening is apparent in the laser ON configuration. (*b*) RBC's stiffness was obtained by fitting the FEC of (*a*) between 7.5 and 12.5 pN. Results are shown for a representative RBC and are reproducible over different RBCs. The error bars are defined as the slope uncertainty of the linear fit. To see this figure in color, go online.

DISCUSSION

RBCs continuously experience mechanical stress in vivo, showing the importance of investigating their mechanical response using biophysical techniques. We have investigated the mechanical deformability and viscoelastic response of RBCs in pulling and force-relaxation experiments in different types of extension-jump protocols. We have found that RBCs exhibit a linear viscoelastic behavior with a triple exponential relaxation function and three well-separated timescales $\tau_F \sim 0.01 - 0.1$ s (fast), $\tau_I \sim 4$ s (intermediate), $\tau_S \sim 70$ s (slow) spanning four decades in time, 0.01–100 s. Most of the literature has focused on the untethered case where there is no tether formation (Fig. 1 *a*) reporting a single exponential with a relaxation time of 0.1–0.6 s (10,15,18,19,25,45–47,61,62), or even two relaxation timescales (48), $\tau_1 = 0.3(2)$ s and $\tau_2 = 19(12)$ s, which are compatible with our fast and intermediate times, $\tau_F = 0.02$–0.3 s and $\tau_I = 4(1)$ s for the untethered case. To our knowledge, no investigation has reported the triple exponential relaxation with three well-defined timescales. The fast timescale τ_F falls in the range of theoretical predictions (0.01–0.1 s) (55,56) and ultrafast microscopy experiments (57). The short time τ_F is also observed when the bead compresses rather than pulls the RBC, $\tau_F = 0.020(5)$ s (*dark green points* in Fig. 4 *c*), excluding the possibility of being an artifact due to the detachment of the bead upon pulling. Relaxation times around the intermediate timescale (1.27–1.5 s) have been also observed, which can be attributed to either the application of a large force (500 pN) or mechanical fatigue (10,22). Moreover, a timescale 10–100 times larger than the fast timescale τ_F has been explained in terms of the reorganization of the spectrin network (56). We hypothesize that the relaxation times reported in the literature combine the fast and intermediate timescales, while τ_F differs in the T and U cases. As a result, both τ_F and τ_I can be linked to the relaxation of the cell membrane, which, according to previous studies, takes place within a few seconds (10,15,18,19,22,25,45–47). Previous relaxation studies on the T case have primarily focused on the length and extrusion velocity of the tether rather than the relaxation times (59), making a direct comparison between timescales difficult. Our experiments show that the value of $\tau_F \sim 0.3$ s in the T case is larger than the timescale observed in the U case, $\tau_F \sim 0.02$ s. Recent investigations have examined the extrusion ($\Delta F > 0$) of membrane tubes on adherent cells, finding relaxation times of 0.3–0.7 s (63) in agreement with our τ_F values for the T case. We have interpreted this as a tether extrusion effect that causes the RBC's membrane to irreversibly flow from the RBC body toward the growing tether, slowing down the fast process and increasing τ_F. Remarkably, and to the best of our knowledge, a $\tau_S \sim 70$ s, for either the U or T cases, has not been reported, probably because of the long time needed for the experiments. What is the origin of the largest timescale τ_S? Dynamical scaling implies that large timescales correspond to larger lengthscales, suggesting that a τ_S of 70 s must arise from a collective process spanning the RBC's body. It is worth noting that other studies of RBC relaxation with optical tweezers have already fitted FRCs to multiple timescales but did not find three distinct timescales and fitted their data to a single power law (27). Furthermore, in systems such as giant vesicles, multiple relaxation timescales have been reported using electro-deformation, in the range of tens of milliseconds to seconds, but not tens of seconds (64,65).

As a further check of the triple exponential behavior we have carried out trap position relaxation experiments using force feedback at 1 kHz after a step force jump is applied (Fig. S10). In this case, we have measured the trap position relaxation curves, finding a triple exponential with more clearly defined relaxation processes. A few relaxational curves are shown in Fig. S11, where a neat triple exponential relaxation and three bumps can be observed by the eye corresponding to the three distinct time-separated relaxational processes.

The triple exponential behavior may look surprising given the large evidence in support of a power law relaxation reported for the creep compliance in mechanical cell experiments (27,33,49–51). Most techniques apply a step jump to the mechanical probe, whether it be the micropipette aspiration pressure, the optical trap position, the AFM cantilever, the magnetic or electric field, the hydrodynamic flow, etc. In many cases, the stress is not kept constant, varying after the stress jump. Our experiments demonstrate that the recovery force ΔF_R grows linearly with the force jump ΔF (Fig. 4 *a* of the main text). Therefore, the relaxation of the force during a compliance creep experiment, even if small (10–20%), mixes the different relaxational processes masking the triple exponential behavior. This is especially true for large force or stress jumps accompanied by a large force or stress relaxation while creep compliance is measured. Our constant force relaxation experiments show three clear distinct time-separated relaxational processes that are incompatible with a power law behavior (supporting material, sections 2.2 and 2.6) confirming this interpretation.

Further evidence of structurally organized relaxational processes in RBCs is observed in relaxation experiments over much longer times, up to half an hour. In Fig. S17, we show one FRC and a fit to four exponentials. Notably, with the extended observation time, we cannot exclude a fourth relaxational time of tens of minutes (Table S7). The existence of different relaxation regimes has also been reported at the level of soft tissues, for instance, in the progression of myocardial infarction (51) where two power law behaviors have been identified. Moreover, a two-step relaxation of RBCs has already been reported in a previous work (48), $\tau_1 = 0.3(2)$ s and $\tau_2 = 19(12)$ s, which are compatible with our fast and intermediate times, $\tau_F = 0.02$–0.3 s and $\tau_I = 4(1)$ s. These findings suggest a potential relation between structured relaxation and biological function at the scale of cells and tissues.

To interpret the origin of the three timescales, we have introduced a viscoelastic model. It shows that the stiffness of the RBC measured in pulling experiments, k_{RBC}, is comparable with the total stiffness of the three viscoelastic processes in a parallel configuration ($k_{\|} = k_F + k_I + k_S$, Fig. 5). Interestingly, the friction coefficients γ_I and γ_S are at least a hundred times larger than γ_F, with and without a tether (Table S6). We interpret the fast process (τ_F) as due to the local dynamics of the membrane, the intermediate process (τ_I) as due to the membrane-cortex interaction, and the slow process (τ_S) to the high cytosol viscosity (>1 Pa $\cdot$ s). What is the current support favoring this interpretation? For the fast timescale τ_F due to the RBC membrane, we note it is the only one that depends on the local geometry of the deformed lipid bilayer between RBC and bead, being larger in the tethered case. Moreover, our ATP-depleted experiments show that, out of the three relaxational processes, only the fast process changes its stiffness and amplitude, k_F and A_F, indicating that the glycolytic activity directly affects the fast process of membrane flickering. Evidence in favor of the slow timescale τ_S as due to the cytosol body comes from measurements of the viscosity of packed RBCs under a shear rate which find values in the range of 1–10 Pa s (66,67), in agreement with our estimates. Indeed, assuming that the RBC is a spherical object of diameter d $\sim 8\ \mu$m, and using the Stokes formula $\gamma_S = 3\pi\eta$ d, we get a viscosity $\eta \sim 2$ Pa s, which is roughly 2000 times the water's viscosity, $\eta \sim 0.001$ Pa s. On the other hand, τ_I and τ_S do not change between the T and U cases because the membrane-cortex and the cytosol deform similarly in the force-relaxation experiments. Finally, upon depleting glucose (Fig. 6), the three timescales decrease, with the stiffness parameters k_F, k_I, and k_S increasing and the friction coefficients γ_F, γ_I, and γ_S decreasing. Therefore, glucose depletion solidifies the RBC by increasing the elastic relative to the viscous response. This result is compatible with the general observation reported in the literature that environmental damage and stress rigidify RBCs. In particular, we have also demonstrated that under light illumination, RBCs become stiffer at a rate that increases with the laser power (Fig. 7).

CONCLUSIONS

Overall, our study reveals structured viscoelastic dynamics. The observed triple exponential behavior with three separated timescales lies in between the pure exponential relaxation observed in linear and two-level systems (68) and the more complex stretched-exponential and power law relaxation observed in polymers, glassy, and amorphous matter (69). We may call this discrete-stretched exponential behavior where the finite number of relaxational timescales is consequential to the organized cell structure. One might ask whether there are other timescales beyond the measured time range in this study ($\sim$5 min), such as the abovementioned fourth timescale of half an hour. Answering this question would require longer experiments in the timescale of hours. Further evidence of structured viscoelastic dynamics is the dynamical scaling observed between the three timescales (Fig. 4 *d*). Although they vary over several orders of magnitude across the RBC population, they mutually scale following a power law, a consequence of the underlying RBC architecture. Future studies should investigate the effect of modifying the lipid bilayer composition and drugs disruptive of the cortex to clarify the current interpretation of the three timescales. Moreover, it would be interesting to explore these relaxational phenomena in other types of RBC (e.g., sickle cell anemia), lymphocytes, and the effect of changing temperature on RBC dynamics.

SUPPORTING MATERIAL

Supporting material can be found online at https://doi.org/10.1016/j.bpj.2024.01.019.

AUTHOR CONTRIBUTIONS

M.G.-T. collected and cured the data, wrote the software for data analysis and took care of visualization, and analyzed the data. F.R. administered the project and supervised the research. M.G.-T. and F.R. wrote the original draft. G.B., R.S., and G.W. discussed the results and implications of the methodology and commented on the manuscript.

ACKNOWLEDGMENTS

M.G.-T. and F.R. are supported by the Spanish Research Council Grant PID2019-111148GB-100. F.R. is supported by the ICREA Academia Prize 2018. R.S. acknowledges support through a Human Frontier Science Program (HFSP) postdoctoral fellowship LT000419/2015. This project has received funding from the European Research Council (ERC) under the European Union's Horizon 2020 research and innovation program (grant agreement no. 883240) to G.W. Moreover, G.W. would like to acknowledge support by the Netherlands Organisation for Scientific Research (NWO/OCW), as part of the BaSyC Gravitation program. We are grateful to N. Gov and A. Hernandez-Machado for a critical reading of the manuscript.

DECLARATION OF INTERESTS

The authors declare no competing interests.

REFERENCES

1. Dean, L. 2005. The ABO blood group.
2. Franco, R. S. 2012. Measurement of red cell lifespan and aging. *Transfus. Med. Hemotherapy.* 39:302–307.
3. Blom, J. A. 2003. Monitoring of Respiration and Circulation. CRC Press.
4. Reichel, F., J. Mauer, …, D. A. Fedosov. 2019. High-throughput microfluidic characterization of erythrocyte shapes and mechanical variability. *Biophys. J.* 117:14–24.
5. Nash, G. B., C. S. Johnson, and H. J. Meiselman. 1984. Mechanical properties of oxygenated red blood cells in sickle cell (HbSS) disease. *Blood.* 63:73–82.
6. Mauritz, J. M. A., A. Esposito, …, C. F. Kaminski. 2010. Biophotonic techniques for the study of malaria-infected red blood cells. *Med. Biol. Eng. Comput.* 48:1055–1063.
7. Vayá, A., R. Alis, …, A. Hernandez-Mijares. 2015. Association of erythrocyte deformability with red blood cell distribution width in metabolic diseases and thalassemia trait. *Clin. Hemorheol. Microcirc.* 61:407–415.
8. Dmitrieff, S., A. Alsina, …, F. J. Nédélec. 2017. Balance of microtubule stiffness and cortical tension determines the size of blood cells with marginal band across species. *Proc. Natl. Acad. Sci. USA.* 114:4418–4423.
9. Inanc, M. T., I. Demirkan, …, M. B. Unlu. 2021. Quantifying the influences of radiation therapy on deformability of human red blood cells by dual-beam optical tweezers. *RSC Adv.* 11:15519–15527.
10. Qiang, Y., J. Liu, …, E. Du. 2019. Mechanical fatigue of human red blood cells. *Proc. Natl. Acad. Sci. USA.* 116:19828–19834.
11. Antonelou, M. H., A. G. Kriebardis, and I. S. Papassideri. 2010. Aging and death signalling in mature red cells: from basic science to transfusion practice. *Blood Transfus.* 8:s39.
12. Arias, C. F., and C. F. Arias. 2017. How do red blood cells know when to die? *R. Soc. Open Sci.* 4, 160850.
13. Embury, S. H., M. R. Clark, …, N. Mohandas. 1984. Concurrent sickle cell anemia and alpha-thalassemia. Effect on pathological properties of sickle erythrocytes. *J. Clin. Invest.* 73:116–123.
14. Liu, J., F. Zhang, …, X. Qu. 2019. Mechanical properties of RBCs under oxidative stress measured by optical tweezers. *Opt Commun.* 442:56–59.
15. Chien, S., K. L. Sung, …, A. Tözeren. 1978. Theoretical and experimental studies on viscoelastic properties of erythrocyte membrane. *Biophys. J.* 24:463–487.
16. Artmann, G. M., K. L. Sung, …, S. Chien. 1997. Micropipette aspiration of human erythrocytes induces echinocytes via membrane phospholipid translocation. *Biophys. J.* 72:1434–1441.
17. Wang, H., P. Obeidy, …, L. A. Ju. 2022. Fluorescence-coupled micropipette aspiration assay to examine calcium mobilization caused by red blood cell mechanosensing. *Eur. Biophys. J.* 51:135–146.
18. Cranston, H. A., C. W. Boylan, …, D. J. Krogstad. 1984. Plasmodium falciparum maturation abolishes physiologic red cell deformability. *Science.* 223:400–403.
19. Artmann, G. 1995. Microscopic photometric quantification of stiffness and relaxation time of red blood cells in a flow chamber. *Biorheology.* 32:553–570.
20. Fedosov, D. A., M. Peltomäki, and G. Gompper. 2014. Deformation and dynamics of red blood cells in flow through cylindrical microchannels. *Soft Matter.* 10:4258–4267.
21. Ciasca, G., M. Papi, …, M. De Spirito. 2015. Mapping viscoelastic properties of healthy and pathological red blood cells at the nanoscale level. *Nanoscale.* 7:17030–17037.
22. Sorkin, R., G. Bergamaschi, …, G. J. L. Wuite. 2018. Probing cellular mechanics with acoustic force spectroscopy. *Mol. Biol. Cell.* 29:2005–2011.
23. Puig-de-Morales-Marinkovic, M., K. T. Turner, …, S. Suresh. 2007. Viscoelasticity of the human red blood cell. *Am. J. Physiol. Cell Physiol.* 293:C597–C605.
24. Henry, E., S. H. Holm, …, G. Gompper. 2016. Sorting cells by their dynamical properties. *Sci. Rep.* 6, 34375.
25. Hénon, S., G. Lenormand, …, F. Gallet. 1999. A new determination of the shear modulus of the human erythrocyte membrane using optical tweezers. *Biophys. J.* 76:1145–1151.
26. Mills, J. P., L. Qie, …, S. Suresh. 2004. Nonlinear elastic and viscoelastic deformation of the human red blood cell with optical tweezers. *Mech. Chem. Biosyst.* 1:169–180.
27. Yoon, Y.-Z., J. Kotar, …, P. Cicuta. 2008. The nonlinear mechanical response of the red blood cell. *Phys. Biol.* 5, 036007.
28. Zhu, R., T. Avsievich, …, I. Meglinski. 2020. Optical tweezers in studies of red blood cells. *Cells.* 9:545.
29. Head, D. A., A. J. Levine, and F. C. MacKintosh. 2003. Deformation of cross-linked semiflexible polymer networks. *Phys. Rev. Lett.* 91, 108102.
30. Mizuno, D., C. Tardin, …, F. C. Mackintosh. 2007. Nonequilibrium mechanics of active cytoskeletal networks. *Science.* 315:370–373.
31. Brochard, F., and J. F. Lennon. 1975. Frequency spectrum of the flicker phenomenon in erythrocytes. *J. Phys. France.* 36:1035–1047.
32. Betz, T., M. Lenz, …, C. Sykes. 2009. ATP-dependent mechanics of red blood cells. *Proc. Natl. Acad. Sci. USA.* 106:15320–15325.
33. Yoon, Y. Z., J. Kotar, …, P. Cicuta. 2011. Red blood cell dynamics: from spontaneous fluctuations to non-linear response. *Soft Matter.* 7:2042–2051.
34. Evans, A. A., B. Bhaduri, …, A. J. Levine. 2017. Geometric localization of thermal fluctuations in red blood cells. *Proc. Natl. Acad. Sci. USA.* 114:2865–2870.
35. Turlier, H., and T. Betz. 2019. Unveiling the Active Nature of Living-Membrane Fluctuations and Mechanics. *Annu. Rev. Condens. Matter Phys.* 10:213–232.
36. Turlier, H., D. A. Fedosov, …, T. Betz. 2016. Equilibrium physics breakdown reveals the active nature of red blood cell flickering. *Nat. Phys.* 12:513–519.
37. Tuvia, S., A. Almagor, …, S. Yedgar. 1997. Cell membrane fluctuations are regulated by medium macroviscosity: evidence for a metabolic driving force. *Proc. Natl. Acad. Sci. USA.* 94:5045–5049.
38. Di Terlizzi, I., M. Gironella, …, F. Ritort. 2023. Variance sum rule for entropy production. Preprint at arXiv. https://doi.org/10.48550/arXiv:2302.08565.
39. Cluitmans, J. C. A., F. Gevi, …, G. J. G. C. M. Bosman. 2016. Red blood cell homeostasis: pharmacological interventions to explore biochemical, morphological and mechanical properties. *Front. Mol. Biosci.* 3:10.

40. Dieterich, E., J. Camunas-Soler, …, F. Ritort. 2015. Single-molecule measurement of the effective temperature in non-equilibrium steady states. *Nat. Phys.* 11:971–977.
41. Gieseler, J., J. R. Gomez-Solano, …, G. Volpe. 2021. Optical tweezers—from calibration to applications: a tutorial. *Adv. Opt. Photonics.* 13:74–241.
42. Chikazumi, S., and C. D. Graham. 2009. Physics of Ferromagnetism 2e, 94. Oxford University Press on Demand.
43. Waugh, R. E., A. Mantalaris, …, J. H. Wu. 2001. Membrane instability in late-stage erythropoiesis. *Blood, The Journal of the American Society of Hematology.* 97:1869–1875.
44. Evans, E. A., and R. M. Hochmuth. 1976. Membrane viscoelasticity. *Biophys. J.* 16:1–11.
45. Hochmuth, R. M., P. R. Worthy, and E. A. Evans. 1979. Red cell extensional recovery and the determination of membrane viscosity. *Biophys. J.* 26:101–114.
46. Bronkhorst, P. J., G. J. Streekstra, …, G. J. Brakenhoff. 1995. A new method to study shape recovery of red blood cells using multiple optical trapping. *Biophys. J.* 69:1666–1673.
47. Dao, M., C. T. Lim, and S. Suresh. 2003. Mechanics of the human red blood cell deformed by optical tweezers. *J. Mech. Phys. Solid.* 51:2259–2280.
48. Braunmüller, S., L. Schmid, …, T. Franke. 2012. Hydrodynamic deformation reveals two coupled modes/time scales of red blood cell relaxation. *Soft Matter.* 8:11240–11248.
49. Kollmannsberger, P., and B. Fabry. 2011. Linear and nonlinear rheology of living cells. *Annu. Rev. Mater. Res.* 41:75–97.
50. Hang, J.-T., Y. Kang, …, H. Gao. 2021. A hierarchical cellular structural model to unravel the universal power-law rheological behavior of living cells. *Nat. Commun.* 12:6067.
51. Chang, Z., J. Zhang, …, G. K. Xu. 2023. New Mechanical Markers for Tracking the Progression of Myocardial Infarction. *Nano Lett.* 23:7350–7357.
52. Wei, M.-T., A. Zaorski, …, H. D. Ou-Yang. 2008. A comparative study of living cell micromechanical properties by oscillatory optical tweezers. *Opt Express.* 16:8594–8603.
53. Lendlein, A., and S. Kelch. 2002. Shape-memory polymers. *Angew. Chem. Int. Ed.* 41:2034–2057.
54. Gov, N. S., and S. A. Safran. 2005. Red blood cell membrane fluctuations and shape controlled by ATP-induced cytoskeletal defects. *Biophys. J.* 88:1859–1874.
55. Gov, N. S. 2007. Active elastic network: cytoskeleton of the red blood cell. *Phys. Rev.* 75, 011921.
56. Ben-Isaac, E., Y. Park, …, Y. Shokef. 2011. Effective temperature of red-blood-cell membrane fluctuations. *Phys. Rev. Lett.* 106, 238103.
57. Rodríguez-García, R., I. López-Montero, …, F. Monroy. 2015. Direct cytoskeleton forces cause membrane softening in red blood cells. *Biophys. J.* 108:2794–2806.
58. Sleep, J., D. Wilson, …, W. Gratzer. 1999. Elasticity of the red cell membrane and its relation to hemolytic disorders: an optical tweezers study. *Biophys. J.* 77:3085–3095.
59. Borghi, N., and F. Brochard-Wyart. 2007. Tether extrusion from red blood cells: integral proteins unbinding from cytoskeleton. *Biophys. J.* 93:1369–1379.
60. Gov, N., J. Cluitmans, …, G. Bosman. 2009. Cytoskeletal control of red blood cell shape: theory and practice of vesicle formation. *Adv. Planar Lipid Bilayers Liposomes.* 10:95–119.
61. Guglietta, F., M. Behr, …, M. Sbragaglia. 2021. Loading and relaxation dynamics of a red blood cell. *Soft Matter.* 17:5978–5990.
62. Li, J. Y., Y. F. Liu, …, B. Z. Mu. 2023. Deformation dynamics of spherical red blood cells in viscous fluid driven by ultrasound. *Environ. Technol.* 35:1–7.
63. Paraschiv, A., T. J. Lagny, …, A. Šarić. 2021. Influence of membrane-cortex linkers on the extrusion of membrane tubes. *Biophys. J.* 120:598–606.
64. Riske, K. A., and R. Dimova. 2005. Electro-deformation and poration of giant vesicles viewed with high temporal resolution. *Biophys. J.* 88:1143–1155.
65. Zhou, H., B. B. Gabilondo, …, W. van de Water. 2011. Stretching and relaxation of vesicles. *Phys. Rev.* 83, 011905.
66. Wells, R., and H. Schmid-Schönbein. 1969. Red cell deformation and fluidity of concentrated cell suspensions. *J. Appl. Physiol.* 27:213–217.
67. Chien, W., G. Gompper, and D. A. Fedosov. 2021. Effect of cytosol viscosity on the flow behavior of red blood cell suspensions in microvessels. *Microcirculation.* 28, e12668.
68. Del Piero, G., and L. Deseri. 1995. Monotonic, completely monotonic, and exponential relaxation functions in linear viscoelasticity. *Q. Appl. Math.* 53:273–300.
69. Yu, Y., M. Wang, …, M. Bauchy. 2015. Stretched exponential relaxation of glasses at low temperature. *Phys. Rev. Lett.* 115, 165901.

Biophysical Journal, Volume *123*

Supplemental information

Viscoelastic phenotyping of red blood cells

Marta Gironella-Torrent, Giulia Bergamaschi, Raya Sorkin, Gijs J.L. Wuite, and Felix Ritort

Supplemental Material for

Viscoelastic phenotyping of red blood cells

Marta Gironella-Torrent, Giulia Bergamaschi, Raya Sorkin, Gijs J.L. Wuite, and Felix Ritort

This PDF contains:

Supplemental Text
Figs. S1 to S20
Tables S1 and S7
Movies S1 and S3

CONTENTS

S1 PULLING EXPERIMENTS

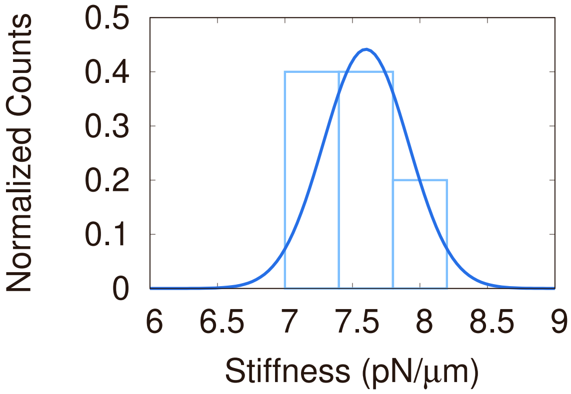

Figure S1: **Creep compliance stiffness histogram.** Stiffness histogram obtained by the inverse of creep compliance evaluated at t = 1s. Gaussian distribution in dark blue solid line. The stiffness value obtained is 7.6(3) pN/μm.

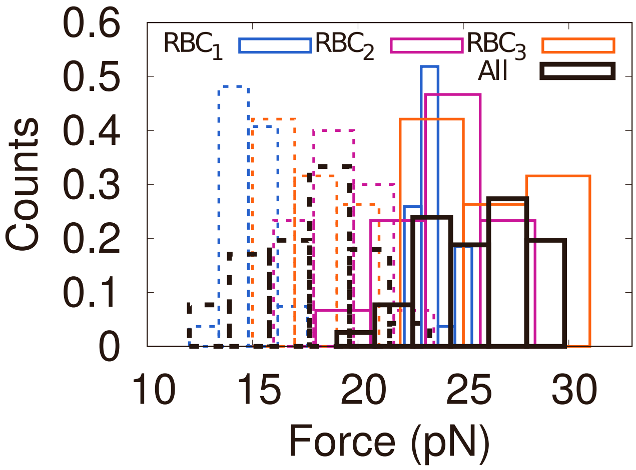

Figure S2: **Force histograms of extrusion/absorption of tether in pulling experiments.** In continuous lines, extrusion force histograms of three different RBCs (colors) together with the total average (black). In dashed lines, absorption force histograms of three different RBCs (colors) together with the total average (black).

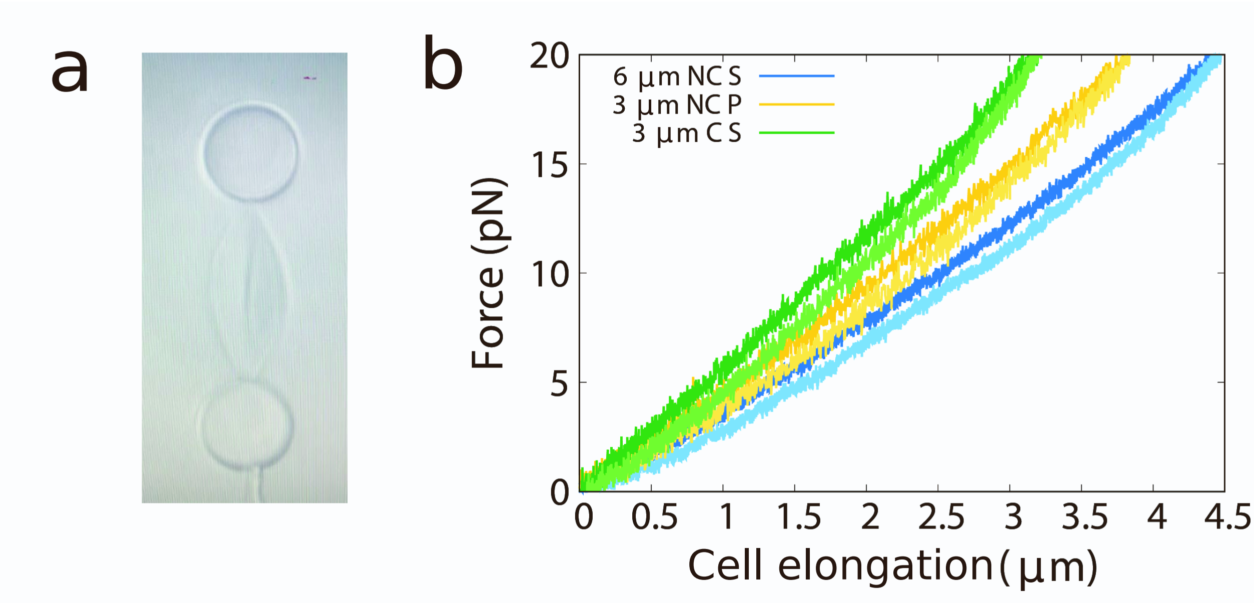

Figure S3: **Coating, size and bead's material in pulling experiments.** Pulling experiments with different bead sizes, coatings and materials. (a) Image of a red blood cell attached to a 6µm diameter silica bead. (b) Pulling curves for three different RBCs with three different conditions. 6µm diameter silica bead without concanavilin coating (blue) $k = 4.5(2)\text{pN}/\mu\text{m}$, 3µm diameter polystyrene bead without concanavilin coating (yellow) $k = 6.3(2)\text{pN}/\mu\text{m}$, and 3µm diameter silica bead with concanavilin coating (green) $k = 6.3(3)\text{pN}/\mu\text{m}$.

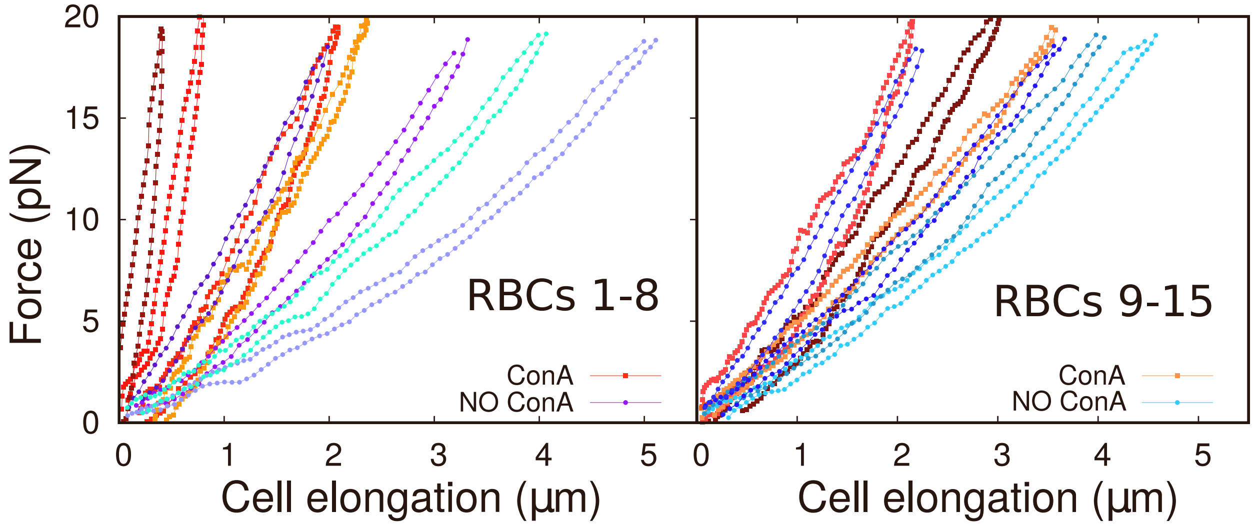

Figure S4: **Concanavilin A coating in pulling experiments.** Force respect to cell elongation for different RBCs. Bluish colors represent force extension curves (FECs) without ConA coating and reddish FECs represent RBCs with ConA coating. The FECs have been divided in two panels indifferently in order to facilitate their visualization.

S2 RELAXATION EXPERIMENTS

S2.1 Force relaxations

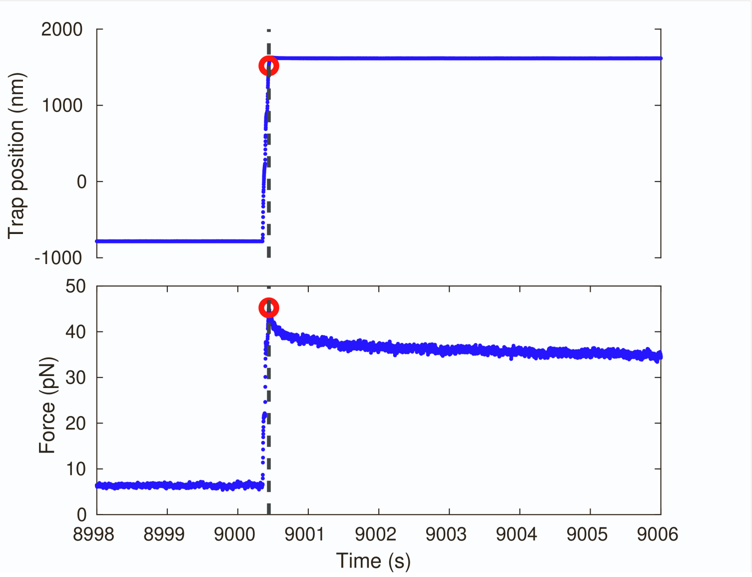

Figure S5: **Initial time for force relaxation curves.** Trap position (upper panel) and force (lower panel) versus time in a force relaxation curve. The initial time (t=0s) is shown in a vertical dashed line and a red circle and is defined as the time where the maximum force is reached.

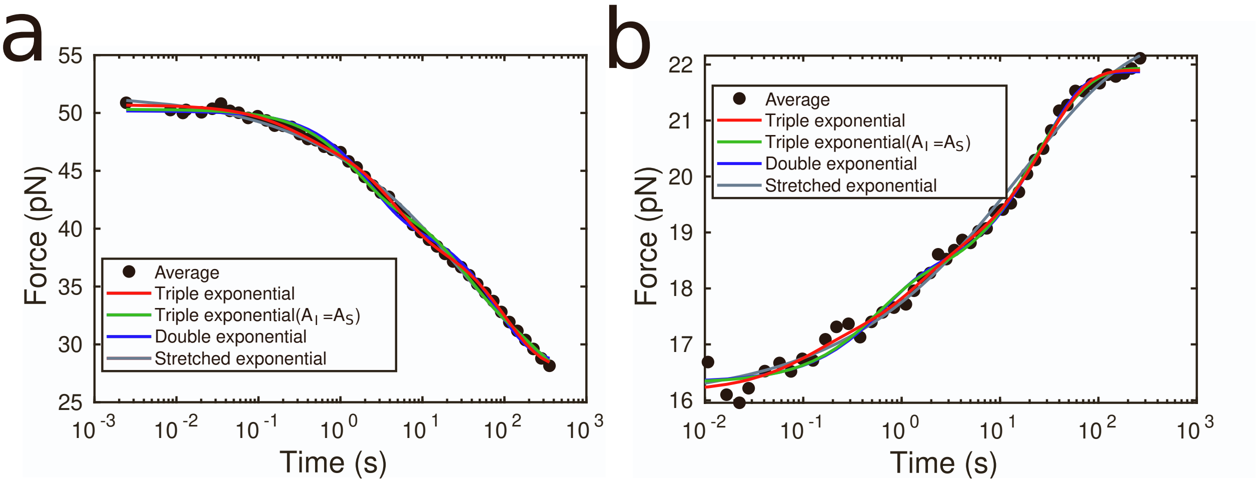

Figure S6: **Force relaxation curve (FRC) with different fits.** Average of the FRC (black points) with fits to triple exponential (red), triple exponential imposing intermediate amplitude equal to slow one (green), double exponential (blue), and stretched exponential (grey). FRCs shown for (**a**) Trotter(+) and (**b**) Ladder(-).

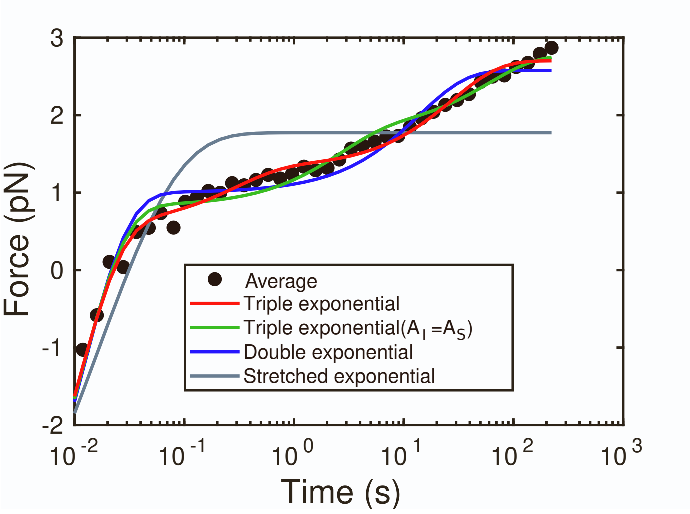

Figure S7: **Force relaxation curve of an ATP-depleted RBC.** Average of the FRC (black points) with fits to triple exponential (red), triple exponential imposing intermediate amplitude equal to slow one (green), double exponential (blue), and stretched exponential (grey). FRC shown for Trotter(-).

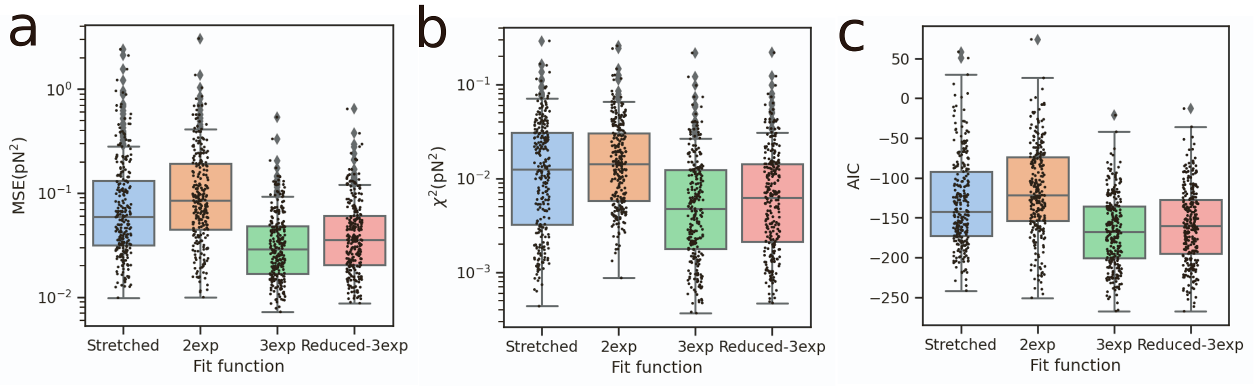

Figure S8: **Statistical tests** to compare fitting functions where each point represents a force relaxation curve. (a) Mean square error. (b) χ^2 . (c) Akaike Information Criterion (AIC).

Table S1: AIC mean and standard error of the mean (SEM) in parenthesis for force relaxation curves (FRCs).

AIC (mean(SEM))	Stretched	2exp	3exp	Reduced 3-exp
FRC	-131(4)	- 116(4)	- 167(3)	-160(3)

Table S2: Statistical tests comparisons between fitting functions for force relaxation curves.

Statistical tests	Mann-Whitney		T-test	
Parameters	score	p-value	score	p-value
Stretched vs 2exp	27863	$4.1\ 10^{-4}$	-2.9	$3.4\ 10^{-3}$
Stretched vs 3exp	45843	$4.1\ 10^{-12}$	8.1	$4.4\ 10^{-15}$
Stretched vs Reduced-3exp	42982	$1.4\ 10^{-7}$	6.2	$8.9\ 10^{-4}$
2exp vs 3exp	51591	$2.6\ 10^{-24}$	11.4	$7.8\ 10^{-27}$
2exp vs Reduced-3exp	49032	$3.7\ 10^{-18}$	9.5	$1.2\ 10^{-19}$
3exp vs Reduced-3exp	30891	0.066	-1.9	0.056

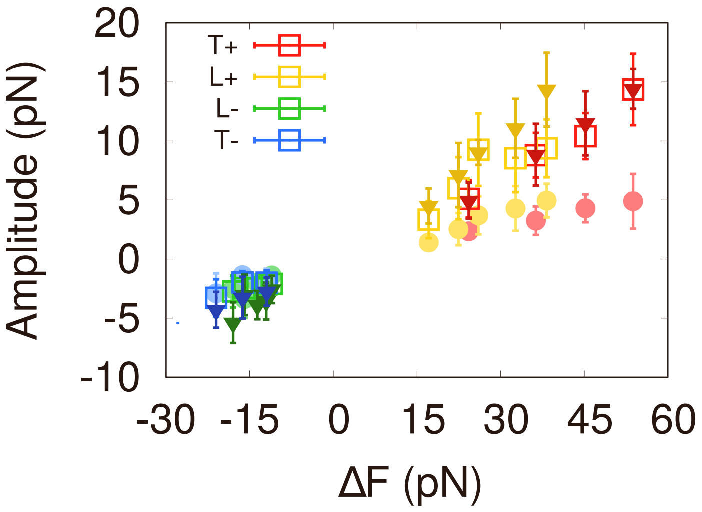

Figure S9: **Amplitudes for the different protocols.** Amplitudes as a function of ΔF for Trotter(+) in red, Ladder(+) in yellow, Trotter(-) in blue, and Ladder(-) in green. Circles represent the fast amplitude, squares represent the intermediate amplitude, and triangles represent the slow amplitude.

S2.2 Trap position relaxations curves (TPRCs)

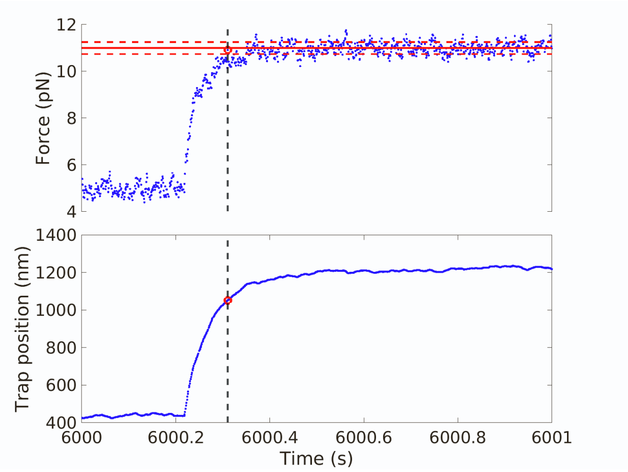

Figure S10: **Initial time for trap position relaxation curves (TPRCs).** Force (upper panel) and trap position (lower panel) versus time in a trap position relaxation curve. The initial time (t=0s) is shown in a vertical dashed line (also red dot) and is defined as the first time the force reaches a value that lies closer than one standard deviation (dashed red lines) with respect to the stationary value of the force (solid red line).

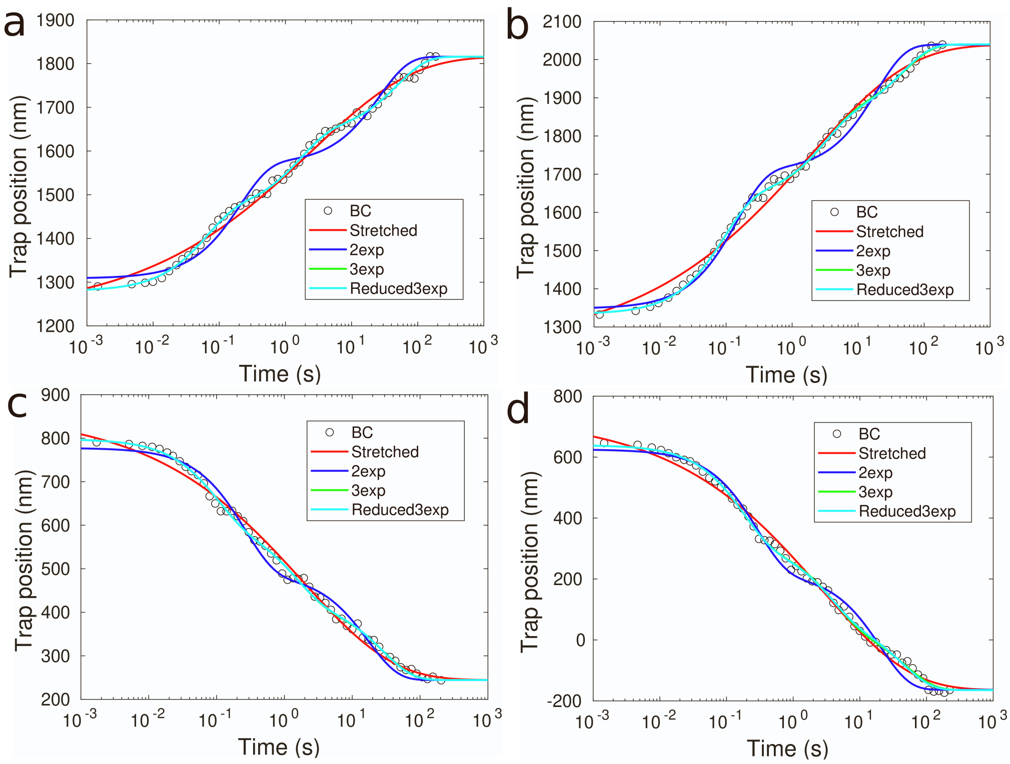

Figure S11: **TPRCs** with the corresponding fits to the four functions. Upper panels forward force jump, $\Delta F > 0$. Lower panels reverse force jump, $\Delta F < 0$.

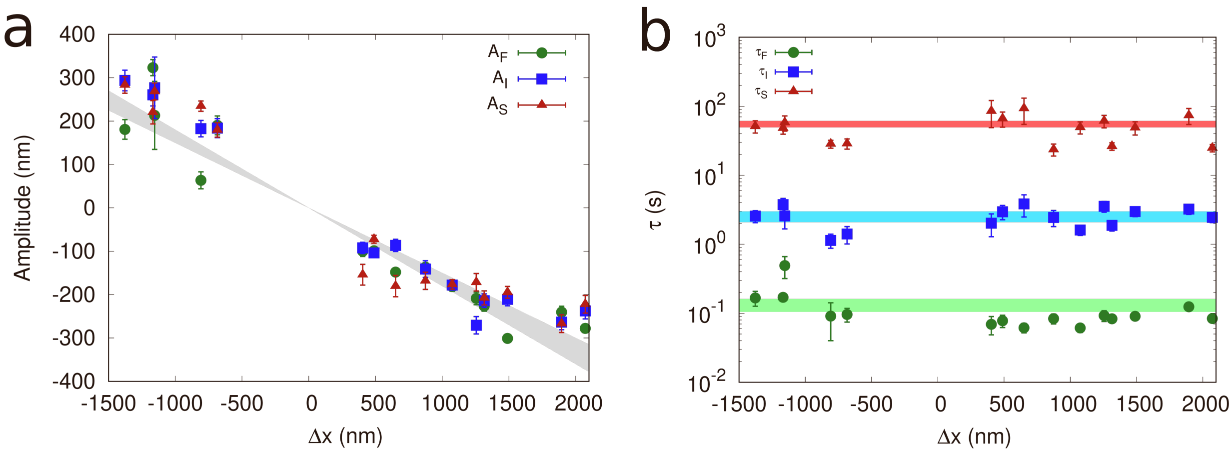

Figure S12: **Fit parameters of TPRCs to a triple exponential.** (a) Amplitudes and (b) Relaxation times versus trap position jump for trap position relaxation curves fitted to a triple exponential function. All the amplitudes are compatible and present a linear dependency with the trap position jump, $A_i/\Delta x = -0.16(2)$ (grey area, panel a), where i = F,I,S. The relaxation times are independent of the trap position jump being τ_F=0.13(3)s, τ_I=2.7(3)s and τ_S=55(6)s.

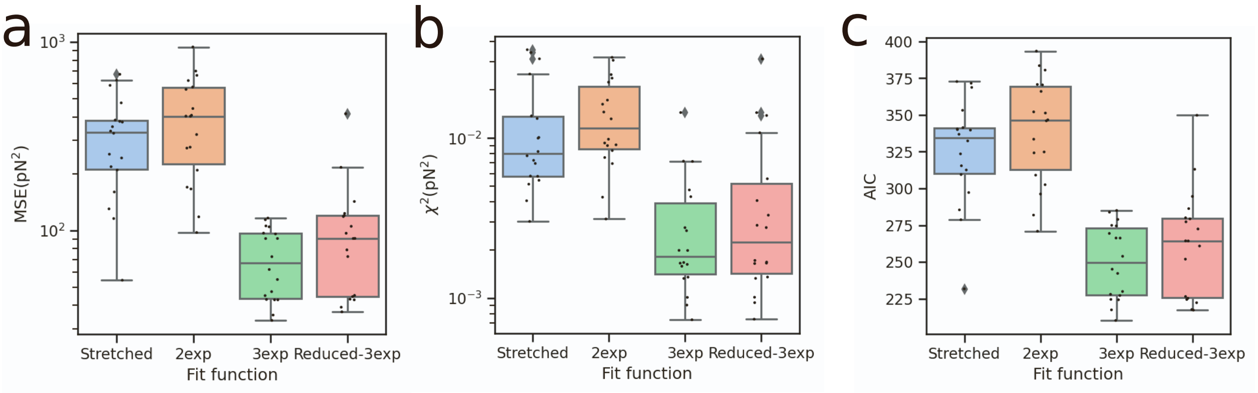

Figure S13: **Statistical tests** to compare fitting functions where each point represents a trap position relaxation curve. (a) Mean square error. (b) χ^2 . (c) Akaike Information Criterion.

Table S3: AIC mean and standard error of the mean (SEM) in parenthesis for trap position relaxation curves (TPRCs).

AIC (mean(SEM))	Stretched	2exp	3exp	Reduced 3-exp
TPRC	325(8)	339(8)	250(6)	263(8)

Table S4: Statistical tests comparisons between fitting functions for trap position relaxation curves.

Statistical tests	Mann-Whitney		T-test	
Parameters	score	p-value	score	p-value
Stretched vs 2exp	128	0.29	-1.2	0.25
Stretched vs 3exp	310	3.110^{-6}	7.2	4.210^{-8}
Stretched vs Reduced-3exp	288	7.110^{-5}	5.2	1.010^{-5}
2exp vs 3exp	317	$1.0\ 10^{-6}$	8.6	1.310^{-9}
2exp vs Reduced-3exp	301	$1.2\ 10^{-5}$	6.3	3.310^{-7}
3exp vs Reduced-3exp	137	0.44	-1.2	0.24

S2.3 Viscoelastic model derivation

We model the RBC by connecting in parallel three Maxwell units (a linear spring and a dashpot in series) with a single linear spring. This way, the viscoelasticity observed in the relaxation experiments, characterized by three exponential processes and a recovery force, is reproduced. In Figure S14, an schematics of the RBC model in the LOT setup is shown.

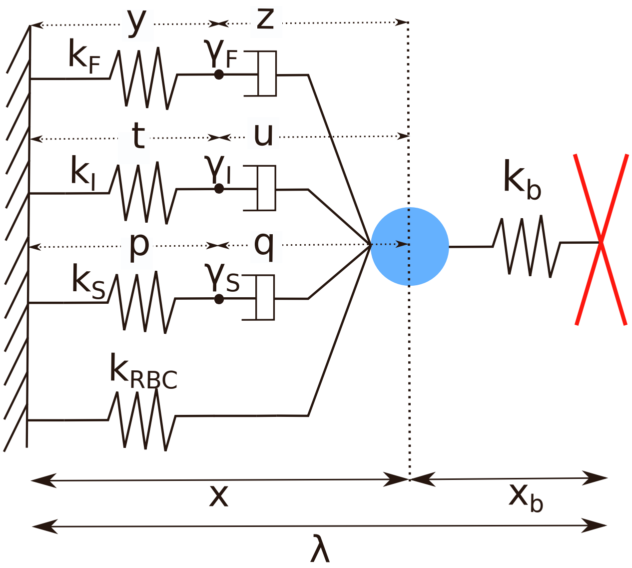

Figure S14: **RBC viscoelastic model based on parallel combination of Maxwell units.**

In this configuration λ is defined as the total distance that results to combined the RBC extension x and the trap extension x_b,

$$\lambda = x + x_b \tag{S1}$$

At the same time, x is the sum between the extension of the spring and the dashpot connected in series for each of the three processes,

$$x = y + z = t + u = p + q \tag{S2}$$

The force exerted to each Maxwell unit is expressed as,

$$f_F = k_F y = \gamma_F \dot{z} \tag{S3}$$

$$f_I = k_I t = \gamma_I \dot{u} \tag{S4}$$

$$f_S = k_S p = \gamma_S \dot{q} \tag{S5}$$

where k_F, k_I and k_S are the springs' stiffness and γ_F, γ_I and γ_S are the dashpots' friction coefficients of the fast, intermediate ans slow processes, and $\dot{z}$, $\dot{u}$ and $\dot{q}$ are the derivatives respect to time of the dashpots extensions. With respect to the optical trap, the exerted force is the product between the trap stiffness k_b and the trap extension x_b,

$$F = k_b x_b = k_b(\lambda - x) \tag{S6}$$

Taking into account that the total force acting on the bead is zero, the force exerted by the optical trap has to be equal to the one exerted by the RBC,

$$F = f_F + f_I + f_S + f_{RBC} \tag{S7}$$

where, $f_{RBC} = k_{RBC}x$, and, therefore combining eqs. S6 and S7 , x is expressed as,

$$x = -\frac{1}{(k_{RBC} + k_b)}(f_F + f_I + f_S - k_b\lambda) \tag{S8}$$

From eq. S3 we get the relation,

$$\dot{y} + \dot{z} = \frac{\dot{f}_F}{k_F} + \frac{f_F}{\gamma_F} \tag{S9}$$

Deriving eqs. S2 and S8 with respect to time and combining them with eq. S9, assuming steady-state conditions, $\dot{\lambda} = 0$, we get for the fast process,

$$-\frac{1}{(k_{RBC} + k_b)}(\dot{f}_F + \dot{f}_I + \dot{f}_S) = \frac{\dot{f}_F}{k_F} + \frac{f_F}{\gamma_F} \tag{S10}$$

Like S10, we obtain two other equivalent equations for the intermediate and slow processes by replacing the rhs of eq. S10 with the slow and intermediate processes ($f_F \longrightarrow f_S, f_I$). By equating the rhs of these three expressions, we rewrite $\dot{f}_I$ in terms of f_I,$\dot{f}_F$ and f_F and $\dot{f}_S$ in terms of f_S,$\dot{f}_F$andf_F, and obtain two independent equations,

$$\dot{f}_I = \frac{k_I}{k_F}\dot{f}_F + \frac{k_I}{\gamma_F}f_F - \frac{k_I}{\gamma_I}f_I \tag{S11}$$

$$\dot{f}_S = \frac{k_S}{k_F}\dot{f}_F + \frac{k_S}{\gamma_F}f_F - \frac{k_S}{\gamma_S}f_S \tag{S12}$$

Substituting eqs. S11 and S12 in the lhs of eq. S10, the latter is rewritten as,

$$-\frac{\dot{f}_F}{k_F}(k_F + k_I + k_S + k_{RBC} + k_b) = \frac{f_F}{\gamma_F}(k_F + k_S + k_{RBC} + k_b) - f_I\frac{k_I}{\gamma_I} - f_S\frac{k_S}{\gamma_S} \tag{S13}$$

To simplify we define the total stiffness as, $k_T = k_F + k_I + k_S + k_{RBC} + k_b$. From eq. S13 we obtain two equivalent but independent equations by permuting the indices $F \leftrightarrow I \leftrightarrow S$. Therefore, we get a generalized equation as,

$$-\frac{\dot{f}_i}{k_i}(k_T) = \frac{f_i}{\gamma_i}(k_T - k_i) - f_j\frac{k_j}{\gamma_j} - f_k\frac{k_k}{\gamma_k} \tag{S14}$$

where i, j, k are different indices for the fast, intermediate and slow processes. To solve eq. S14 we assume well-separated time scales. For the fast process, we assume that in the slow and intermediate processes the forces have not yet relaxed and therefore $\dot{f}_I = \dot{f}_S = 0$ and hence f_I, f_S can be taken as constants,

$$-\frac{\dot{f}_F}{k_F}(k_T) = \frac{f_F}{\gamma_F}(k_T - k_F) - f_I\frac{k_I}{\gamma_I} - f_S\frac{k_S}{\gamma_S} \tag{S15}$$

A similar argument for the intermediate and the slow processes yield to a generalize expression for the relaxation time,

$$\tau_i = \frac{\gamma_i k_T}{k_i(k_T - k_i)} \tag{S16}$$

The force amplitude of each spring-dashpot process is defined as,

$$f_i = k_i \Delta x \tag{S17}$$

Combining eqs. S17 and S7, we can express the displacement in terms of the force jump, ΔF as,

$$\Delta x = \frac{\Delta F}{k_{RBC} + k_{||}} \tag{S18}$$

where a $k_{||} = k_F + k_I + k_S$. Therefore, substituting eq. S18 in eq. S17, we get the generalize expression for the amplitudes in terms of ΔF,

$$f_i = \frac{k_i}{k_{RBC} + k_{||}} \Delta F \tag{S19}$$

We define the recovery force ΔF_R as,

$$\Delta F_R = \Delta F - \Delta F' \tag{S20}$$

where ΔF is the force jump and $\Delta F'$ is the difference between the force after the five minutes relaxation, F_f, and the force before the jump, F_i ($\Delta F' = F_f - F_i$) which can also be expressed as,

$$\Delta F' = k_{RBC} \Delta x' \tag{S21}$$

Then, as $\Delta F' = k_b(\Delta\lambda - \Delta x')$, we get the corresponding displacement $\Delta x'$ in terms of $\Delta\lambda$,

$$\Delta x' = \frac{k_b}{k_{RBC} + k_b} \Delta\lambda \tag{S22}$$

Substituting eq. S22 in eq. S21, we get,

$$\Delta F' = \frac{k_{RBC} k_b}{k_{RBC} + k_b} \Delta\lambda \tag{S23}$$

To obtain $\Delta\lambda(\Delta F)$, we substitute eq. S18 in $\Delta F = k_b(\Delta\lambda - \Delta x)$, obtained from the rhs of eq. S6,

$$\Delta\lambda = \frac{k_{RBC} + k_{||} + k_b}{k_b(k_{RBC} + k_{||})} \Delta F \tag{S24}$$

Substituting eq. S24 in eq. S23, we obtain $\Delta F'$ in terms of ΔF,

$$\Delta F' = \frac{k_T}{(k_b(k_T - k_b))} \frac{k_{RBC} k_b}{(k_{RBC} + k_b)} \Delta F \tag{S25}$$

Then the recovery force can be expressed as,

$$\Delta F_R = \Delta F(1 - \frac{k_T}{(k_b(k_T - k_b))} \frac{k_{RBC} k_b}{(k_{RBC} + k_b)}) \tag{S26}$$

Simplifying eq. S26, we obtain the final expression for the recovery force,

$$\Delta F_R = \frac{\Delta F}{(1 + \frac{k_{RBC}}{k_b})(1 + \frac{k_{RBC}}{k_{||}})} \tag{S27}$$

S2.4 ATP depletion

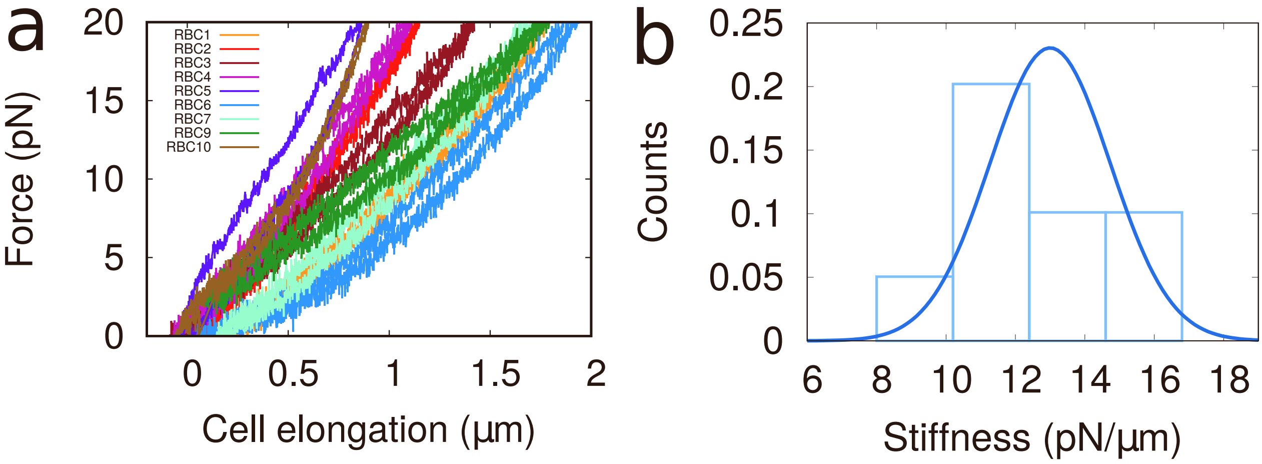

Figure S15: **ATP-depleted RBC pulling experiments.** (a) Force extension curves of 10 different ATP-depleted RBCs. (b) Histogram of RBCs stiffness. The cell stiffness is obtained by performing a linear fit between 7.5pN and 12.5pN in the FEC.

Table S5: Amplitudes and relaxation times of healthy and treated RBCs from force relaxation curves.

	$A_F/\Delta F$	$A_I/\Delta F$	$A_S/\Delta F$	τ_F (s)	τ_I (s)	τ_S (s)
Healthy Untethered	0.11(1)	0.15(2)	0.15(2)	0.020(5)	4(1)	70(8)
Healthy Tethered	0.11(1)	0.27(3)	0.27(3)	0.020(5)/ 0.30(5)	4(1)	70(8)
Treated Tethered	0.31(3)	0.20(3)	0.20(3)	0.029(2)	1(1)	41(3)

Table S6: Stiffnesses and friction coefficients obtained by solving Eqs. S16,S19,S27.

	pN/μm					pN $\cdot$ s/μm		
	k_{RBC}	$k_{\|\|}$	k_F	k_I	k_S	γ_F	γ_I	γ_s
Healthy Untethered	6.1(13)	5.3(1)	1.3(1)	2.0(1)	2.0(1)	0.025(3)	7.8(6)	136(12)
Healthy Tethered	2.7(6)	6.4(4)	1.0(1)	2.7(5)	2.7(5)	0.29(2)	10.2(7)	179(13)
Treated Untethered	13(3)	-	-	-	-	-	-	-
Treated Tethered	6(2)	8.9(4)	3.7(6)	2.6(3)	2.6(3)	0.10(2)	2.5(3)	101(10)

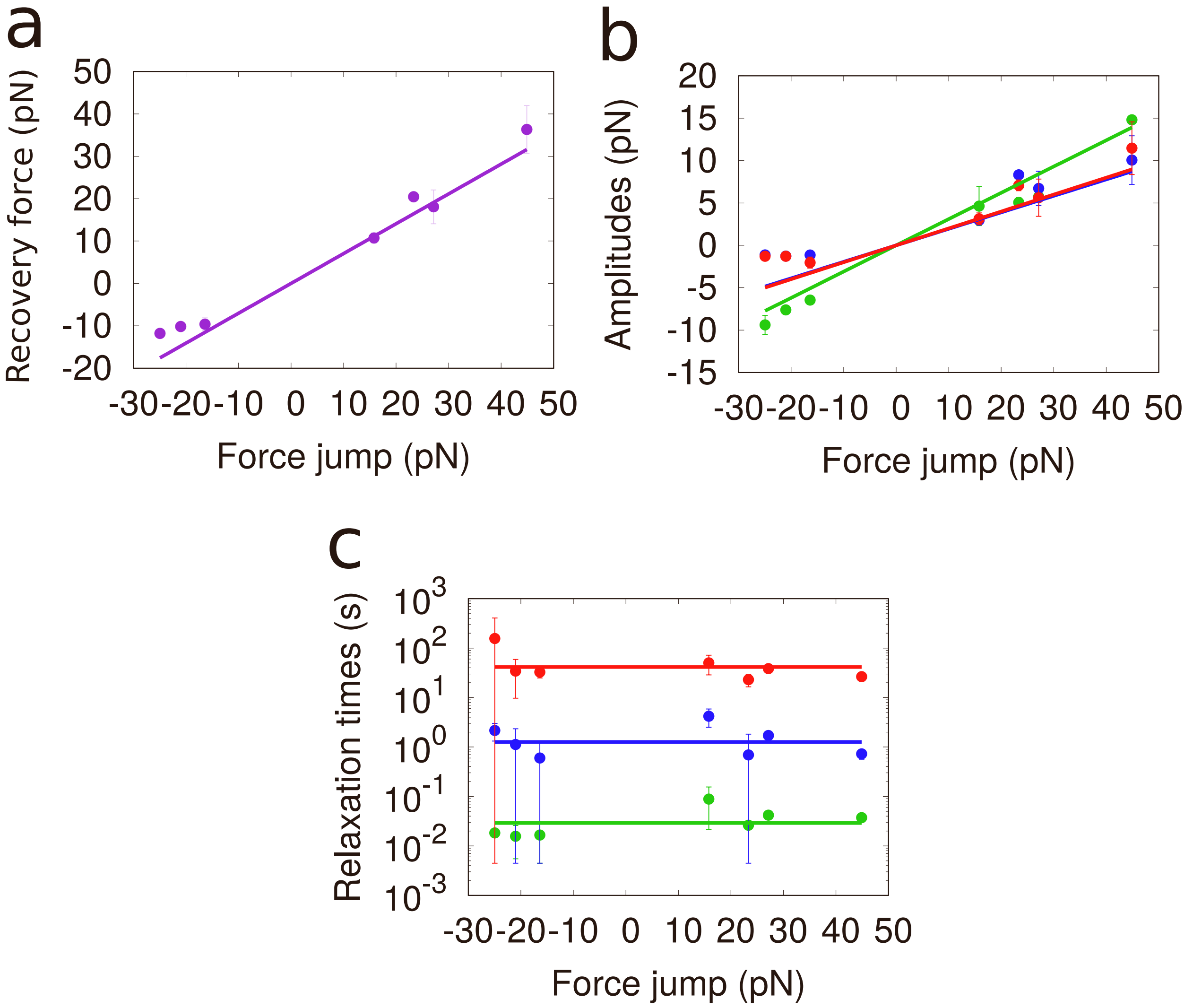

Figure S16: **ATP-depleted RBC relaxation parameters.** (a) Recovery force versus jump force with the corresponding linear fit. (b) Amplitudes versus jump force with their corresponding linear fits. (c) Relaxation times versus jump force with their corresponding fits to a constant value.

S2.5 Long Relaxation

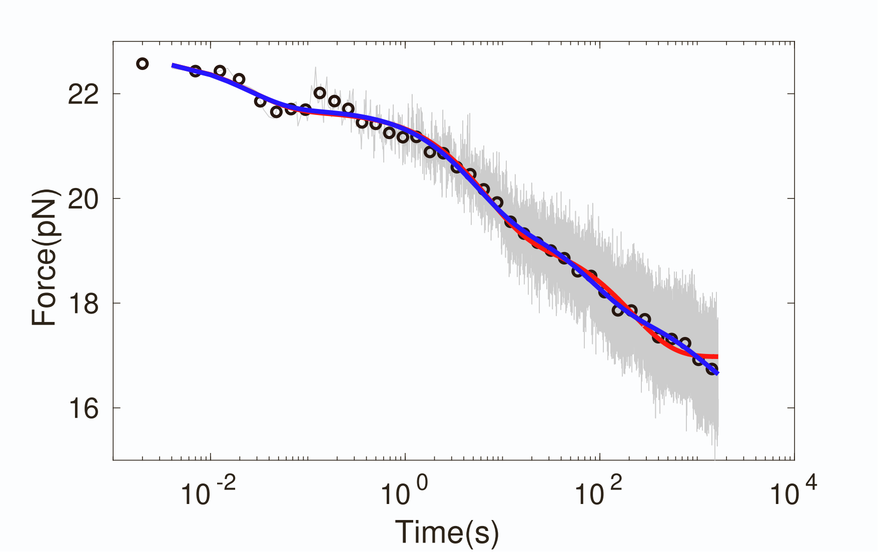

Figure S17: **Long force relaxation curve.** Long relaxation upon 1500 seconds. Fit to three exponentials in red and to four exponentials in blue.

Table S7: Fitting parameters for a triple exponential and a quadruple exponential for a long force relaxation curve.

	$A_F/\Delta F$	τ_F(s)	$A_I/\Delta F$	τ_I(s)	$A_S/\Delta F$	τ_S(s)	$A_L/\Delta F$	τ_L(s)
3exp	1.0(2)	0.026(15)	2.0(4)	7(1)	2.3(2)	210(60)	-	-
4exp	1.0(2)	0.024(13)	2.0(2)	5(1)	1.7(7)	75(20)	1.8(9)	1300(500)

S2.6 Power Law fits

As mention in the section Discussion and Conclusions, there is large evidence in support of a power law relaxation. For that reason, in this section we show different power law fits to our data.

In [27, 33], the authors perform force relaxation experiments and fit a power law to the stiffness variation which is defined as,

$$k(t) = (F(t) - F_i)/\Delta L(t) \tag{S28}$$

with $L(t) = L(t) - L_0$, the RBC extension previous to the jump. After the jump at t=0, the optical trap position is kept at a fixed position so $\Delta\lambda = 0$. For $t > 0$ both the force $F(t)$ and RBC extension $L(t)$ relax toward their stationary values. In our setup we do not directly measure $L(t)$, however we can determine the change in RBC extension using the relation, $\Delta L(t) = \Delta\lambda - \Delta x_b$. During the relaxation $\Delta\lambda = 0$ so $\Delta\lambda(t) = -\Delta x_b(t)$, that can be expressed in terms of the force and the trap stiffness, k_b, as $\Delta L(t) = (F(0) - F(t))/k_b$.

$$k(t) = (F(t) - F_i)/(F(0) - F(t))/k_b) = k_b(F_s - F_i)/(F(0) - F_s) + \Delta k(t) = const + \Delta k(t) \tag{S29}$$

with $F_s = F(\infty)$ the stationary force. The constant and $k(t)$ are given by,

$$const = k_b(F_s - F_i)/(F(0) - F_s)) \tag{S30}$$

and

$$\Delta k(t) = k_b[(F(t) - F_i)/(F(0) - F(t))/k_b) - (F_s - F_i)/(F(0) - F_s))] \tag{S31}$$

According to references [27, 33] the time dependent part of the stiffness $\Delta k(t)$ follows a power law behavior,

$$\Delta k(t) = \Delta k_0 (t/t_0)^{-\alpha} \tag{S32}$$

with $\alpha > 0$ and Δk_0 a constant. In Figure S18, we show the experimental data and the fit using Eq. S32.

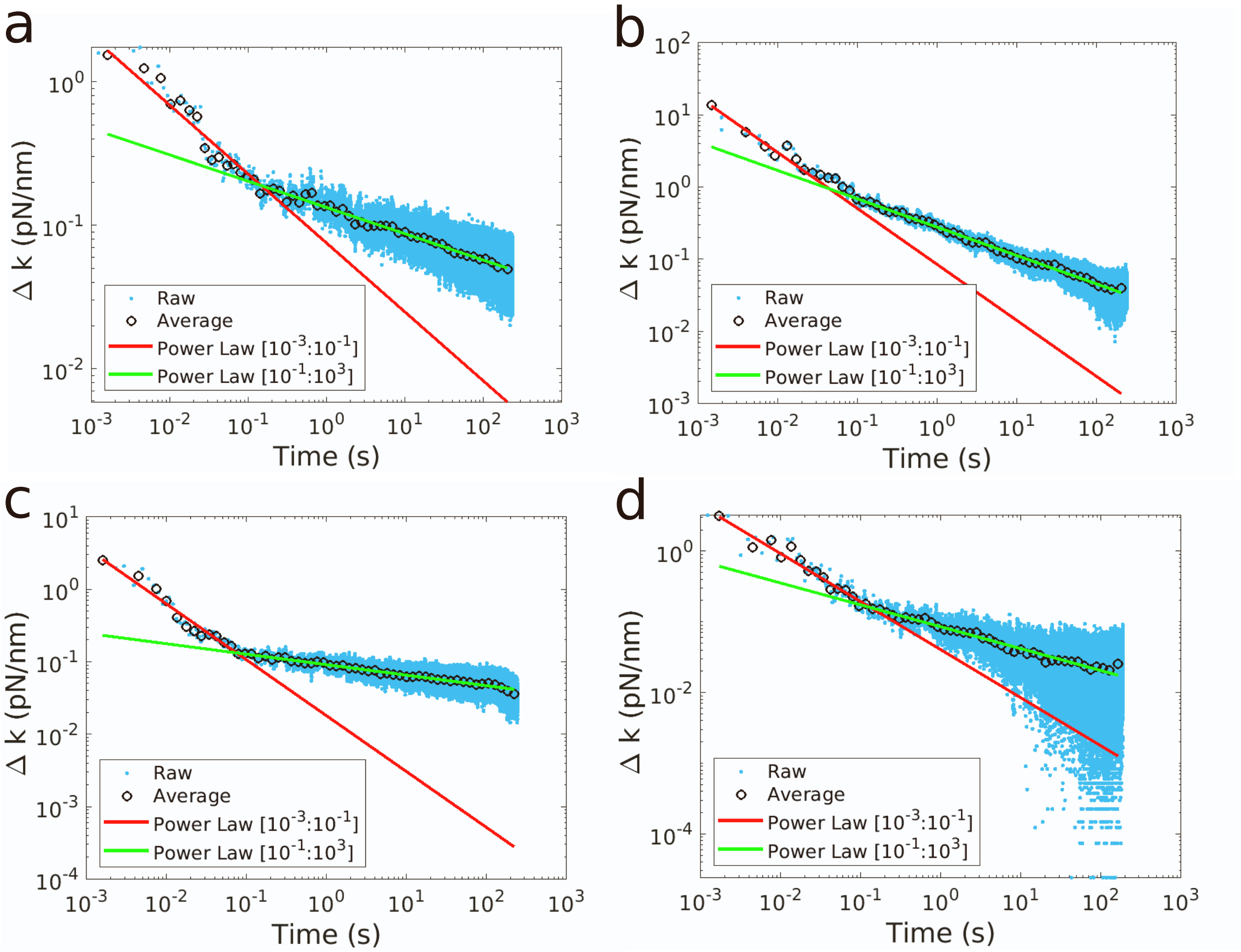

Figure S18: **Stiffness variation power law.** Stiffness variation with respect to time for two reverse (upper panels) and two forward (lower panels) relaxations. Raw data (blue), average (black circles), fit to Eq. S32 for whole time range (red solid line) and for range between 0.1s and 100s (green solid line).

In other references as [49, 50]. We have also considered the power law fit to the TPRCs at constant force, as suggested by the reviewer. The creep compliance J(t) is defined as,

$$J(t) = x(t)/\Delta F \tag{S33}$$

where $x(t) = x(t) - x(0)$ with $t = 0$s the time after the step jump force ΔF is applied. $t = 0$ equals the first time at which the force reaches a value that lies closer than one standard deviation from the stationary value of the force (Fig. S10, red circle and solid red line). In Figure S19, we show four TPRCs with the corresponding power law fit,

$$J(t) = j_0(t/\tau_0)^{\beta} \tag{S34}$$

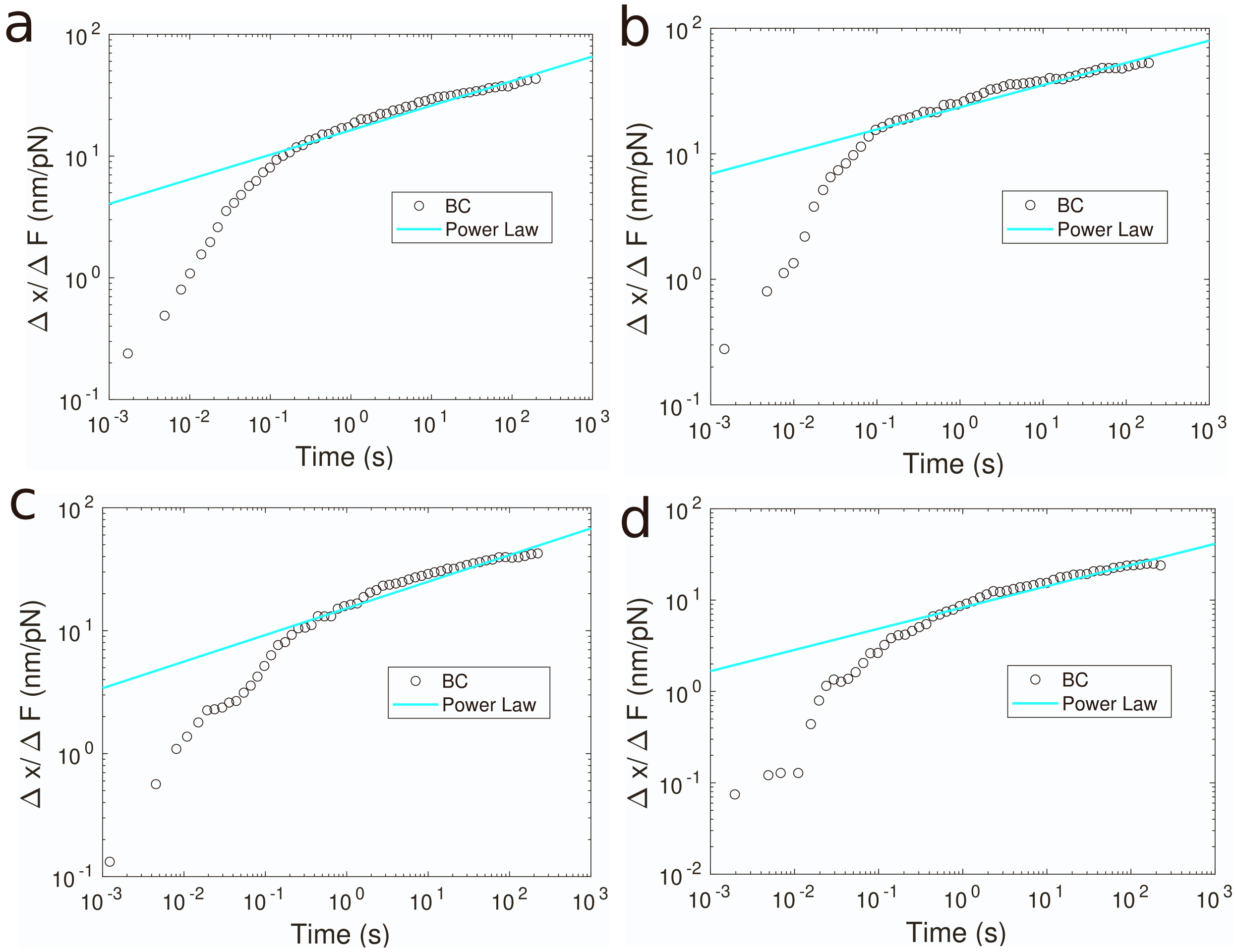

Figure S19: **Power law fit to creep compliance.** Creep compliance versus time for four trap position relaxation curves. Average data in black circles and fit a power law (Eq. S34) in cyan solid line. Forward force jumps (F>0) in upper panels and reverse force jumps (F<0) in lower panels.

In Ref. [51], the authors used two power laws, each one to fit a decade of time. The first power law adjusts the time decade from 0.01 to 0.1s and the second one from 1s to 10s. In Figure S20, we show our data fitted to two power laws using the same time ranges.

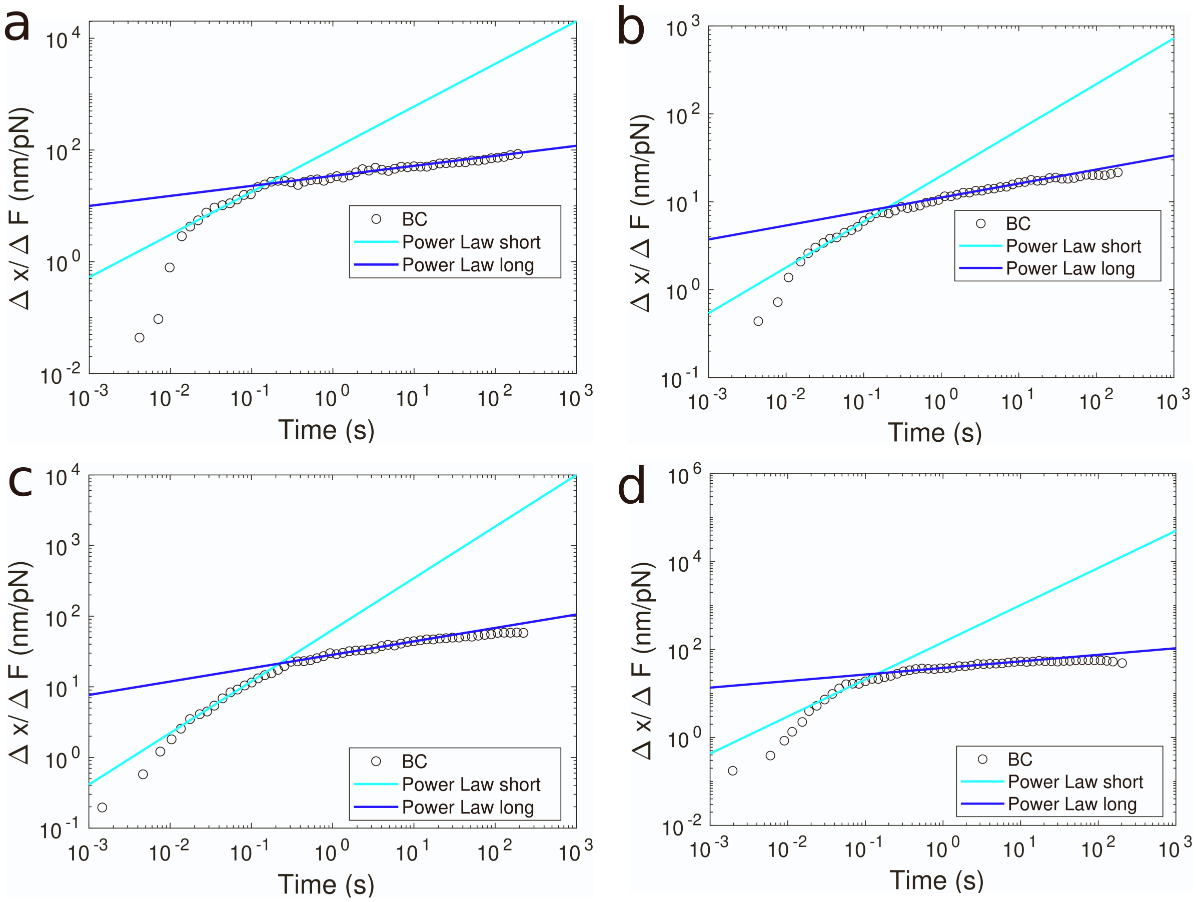

Figure S20: **Two power law fit to creep compliance.** Creep compliance versus time for four trap position relaxation curves. Average data in black circles, fit to the long times power law in dark blue solid line and fit to the short times power law in cyan solid line. Forward force jumps (F>0) in upper panels and reverse force jumps (F<0) in lower panels.

As we can see from Figures S18,S19, and S20, the power law behavior Eqs. S32 is not observed over the 5-6 decades of time of the experiments. In contrast, a power law fit between 0.1s and 300s works reasonably well.

S2.7 Movies

Movie S1: **Formation of a tether in a tensional relaxational experiment.** A very thin tether hardly observable is former upon increasing the force ($\Delta F > 0$) and stretching the RBC after sudden movement of the pipette downwards at time 3 seconds after starting the movie.

Movie S2: **Formation of a tether in a compressional relaxational experiment.** A thicker observable tether is former upon reducing the force ($\Delta F < 0$) and compressing the RBC after sudden movement of the pipette upwards at time 3 seconds after starting the movie.

Movie S3: **Effect of laser illumination on an optically trapped RBC.** It can be observed that the RBC membrane breaks and releases body content. RBC material is observed to be released at time 29 seconds after starting the movie.